

Thesis for the Degree of Licentiate of Engineering

# Quantitative studies of changes in microstructure and activity during ageing of supported catalysts

Torben Pingel



**CHALMERS**

Department of Applied Physics

Chalmers University of Technology

Gothenburg, Sweden 2015

Quantitative studies of changes in microstructure and activity during ageing of  
supported catalysts  
Torben Pingel

© Torben Pingel, 2015.

Department of Applied Physics  
Chalmers University of Technology  
412 96 Gothenburg  
Sweden  
Telephone +46 (0)31-772 3325

Cover picture:

**Upper left:** STEM image of Pt-Pd nanoparticles and clusters of an untreated Pt-Pd/Al<sub>2</sub>O<sub>3</sub> catalyst. **Upper right:** STEM image of a Pt-Pd nanoparticle after ageing at 800 °C. **Center:** SEM image of Pt-Pd nanoparticles on an alumina particle after ageing at 600 °C. **Lower left:** CO oxidation versus temperature curve of a fresh Pt-Pd/Al<sub>2</sub>O<sub>3</sub> catalyst. **Lower right:** Nanoparticle size distribution from the outer layer of an alumina support particle after ageing at 500 °C.

Printed at Chalmers Reproservice  
Gothenburg, Sweden 2015

Quantitative studies of changes in microstructure and activity during ageing of supported catalysts

Torben Pingel  
Department of Applied Physics  
Chalmers University of Technology

## Abstract

Catalytic converters have substantially contributed to the improvement of air quality in populated areas in the last decades by abatement of the emission of hazardous components such as CO, unburned hydrocarbons and NO<sub>x</sub>. However, due to the exposure to high temperature and different components in the exhaust gas, the performance of the catalysts degrades with time. An understanding of the microstructural and chemical changes of the catalysts during different operating conditions is required in order to develop strategies to reduce the degradation.

In the present work, a bimetallic Pt-Pd nanoparticle catalyst supported on  $\gamma$ -alumina was investigated using high resolution electron microscopy and spectroscopy. The studies included both fresh and aged catalyst systems. In order to allow a quantitative evaluation of the particle size distributions and locations on the support, a new TEM specimen preparation method was developed. The new method allows for monitoring the evolution of the particle size distribution as well as the spatial difference in the porous oxide support. These microstructural observations were complemented by investigations of the chemical composition and alloying of the nanoparticles. Finally, CO oxidation experiments were performed to correlate the observed microstructural and compositional changes to the catalytic activity.

**Keywords:** supported nanoparticle catalyst; transmission electron microscopy (TEM); scanning electron microscopy (SEM); FIB/SEM; quantitative; particle size distribution (PSD); specimen preparation; ageing properties; bimetallic catalyst; CO oxidation





## List of appended papers

This thesis is based on the following papers:

### Paper I

*Specimen preparation method to reveal the spatial distribution of nanoparticles in supported catalysts by transmission electron microscopy*

Torben Pingel, Magnus Skoglundh, Henrik Grönbeck, Eva Olsson

Submitted to *Journal of Microscopy*

### Paper II

*Correlation between catalytic activity and microstructure of a pristine and aged Pt-Pd/Al<sub>2</sub>O<sub>3</sub> automotive emission control catalyst*

Torben Pingel, Sheedeh Fouladvand, Peter Westenberger, Daniel Phifer, Magnus Skoglundh, Henrik Grönbeck, Eva Olsson

In manuscript

My contribution to the appended papers:

Paper I: I performed all the experimental work, interpreted the results together with my co-authors, wrote the first draft and wrote the manuscript together with my co-authors.

Paper II: I performed the catalyst ageing procedure, TEM specimen preparation, all SEM and TEM experiments and corresponding data analysis and interpreted the results of those measurements as well as the FIB/SEM experiments and the catalytic activity tests together with my co-authors. I wrote the first draft and wrote the manuscript together with my co-authors.

In addition to the above papers, I contributed to the following published papers, which are not included in this thesis:

*The effect gas composition during thermal aging on the dispersion and NO oxidation activity over Pt/Al<sub>2</sub>O<sub>3</sub> catalysts*

Xavier Auvray, Torben Pingel, Eva Olsson, Louise Olsson  
*Applied Catalysis B: Environmental*, 129, 517–527, 2013.

*Mechanisms behind sulfur promoted oxidation of methane*

Djamela Bounechada, Sheedeh Fouladvand, Lisa Kylhammar, Torben Pingel, Eva Olsson, Magnus Skoglundh, Johan Gustafson, Marco Di Michiel, Mark A. Newton, Per-Anders Carlsson  
*Phys. Chem. Chem. Phys.*, 15, 8648, 2013.

*Methane Oxidation Over Pd Supported on Ceria–Alumina Under Rich/Lean Cycling Conditions*

Sheedeh Fouladvand, Stefan Schernich, Jörg Libuda, Henrik Grönbeck, Torben Pingel, Eva Olsson, Magnus Skoglundh, Per-Anders Carlsson  
*Top. Catal.*, 56, 410–415, 2013.

*On the performance of Ag/Al<sub>2</sub>O<sub>3</sub> as a HC-SCR catalyst – influence of silver loading, morphology and nature of the reductant*

Hannes Kannisto, Kalle Arve, Torben Pingel, Anders Hellman, Hanna Härelind, Kari Eränen, Eva Olsson, Magnus Skoglundh, Dmitry Yu. Murzin  
*Catal. Sci. Technol.*, 3, 644, 2013.

*Thermodynamics of hydride formation and decomposition in supported sub-10 nm Pd nanoparticles of different sizes*

Carl Wadell, Torben Pingel, Eva Olsson, Igor Zoric, Vladimir P. Zhdanov, Christoph Langhammer  
*Chemical Physics Letters*, 603, 75–81, 2014.

# Contents

<b>List of Figures</b>	<b>ix</b>
<b>List of Tables</b>	<b>x</b>
<b>List of abbreviations</b>	<b>xi</b>
<b>1 Introduction</b>	<b>1</b>
<b>2 Heterogeneous catalysis and deactivation</b>	<b>3</b>
2.1 Heterogeneous catalysis . . . . .	3
2.2 Automotive catalytic converters . . . . .	5
2.3 Catalyst deactivation mechanisms . . . . .	8
2.4 Bimetallic Pt-Pd catalysts . . . . .	11
<b>3 Materials and methods</b>	<b>13</b>
3.1 Catalyst sample . . . . .	13
3.2 Hydrothermal ageing . . . . .	13
3.3 Surface area measurements (BET method) . . . . .	15
3.4 Catalytic activity evaluation: CO oxidation . . . . .	15
3.5 Scanning electron microscopy (SEM) . . . . .	16
3.6 Scanning transmission electron microscopy (STEM) . . . . .	18
3.6.1 Imaging principle . . . . .	18
3.6.2 Resolution and aberrations . . . . .	20
3.6.3 Electron beam damage . . . . .	22
3.6.4 Instrumentation . . . . .	23
3.7 Particle size analysis . . . . .	23
3.8 Energy-dispersive X-ray (EDX) spectroscopy . . . . .	24
3.9 Focused ion beam / scanning electron microscopy (FIB/SEM) . . . . .	26
3.9.1 FIB/SEM TEM specimen preparation . . . . .	27
3.9.2 FIB/SEM slice & view . . . . .	27
<b>4 TEM specimen preparation</b>	<b>29</b>
4.1 Traditional crushing method . . . . .	29
4.2 Dimple grinding and argon ion milling . . . . .	31
4.3 FIB/SEM lift-out method . . . . .	33

<b>5</b>	<b>Ageing studies</b>	<b>39</b>
5.1	High-resolution STEM imaging of crushed specimens . . . . .	39
5.2	Nanoparticle sizes and distribution - STEM investigation . . . . .	42
5.3	Nanoparticle sizes and distribution - SEM investigation . . . . .	45
5.4	Three-dimensional nanoparticle distribution - FIB/SEM slice & view	47
5.5	Chemical characterisation by EDX . . . . .	49
5.6	Surface area measurement (BET method) . . . . .	54
5.7	Activity evaluation by CO oxidation . . . . .	55
<b>6</b>	<b>Conclusions and outlook</b>	<b>59</b>
	<b>Acknowledgments</b>	<b>61</b>
	<b>Bibliography</b>	<b>63</b>

## List of Figures

2.1	Schematic of the elementary steps of a catalysed Langmuir-Hinshelwood CO oxidation. . . . .	4
2.2	Structure of an automotive catalytic converter at different length scales. . . . .	7
2.3	European emission legislation for diesel passenger cars from 1992 to 2014. . . . .	8
2.4	Schematic view of different catalyst deactivation mechanisms. . . . .	9
3.1	Reactor set-up for synthetic ageing. . . . .	14
3.2	Schematic drawing showing the different signals commonly used in SEM. . . . .	18
3.3	Schematic drawing illustrating different signals in STEM imaging. . . . .	20
3.4	Process of creating PSDs from SEM and TEM images. . . . .	24
3.5	Schematic drawing of the principal setup of a FIB/SEM during ion milling. . . . .	26
4.1	STEM image of an alumina support fragment produced by the traditional crushing method. . . . .	30
4.2	HAADF-STEM images of a Pt-Pd/Al <sub>2</sub> O <sub>3</sub> catalyst prepared by the traditional crushing method. . . . .	31
4.3	Specimen preparation by dimple grinding and argon ion milling. . . . .	32
4.4	Specimen preparation by FIB/SEM lift-out. . . . .	34
4.5	Results obtained from a Pt-Pd/Al <sub>2</sub> O <sub>3</sub> catalyst prepared for TEM by the FIB/SEM lift-out method. . . . .	36
5.1	HAADF-STEM images of the fresh and aged specimens (700 °C and 800 °C) prepared by the traditional crushing method. . . . .	40
5.2	HAADF-STEM image series demonstrating beam damage to small nanoparticles. . . . .	41
5.3	HAADF-STEM images of the fresh and aged specimen prepared by the FIB/SEM lift-out method. . . . .	43
5.4	PSDs obtained from STEM images of the fresh as well as 500 °C and 600 °C aged specimen. . . . .	44
5.5	SEM images and corresponding PSDs of the fresh and aged specimens embedded in resin. . . . .	46
5.6	Results from a FIB/SEM slice & view measurement of the fresh specimen. . . . .	48
5.7	HAADF-STEM image and EDX concentration maps of a region of the fresh sample containing several large Pt-Pd nanoparticles. . . . .	50
5.8	HAADF-STEM images and EDX concentration maps of nanoparticles in the sample aged at 800 °C. . . . .	51

5.9	EDX spectra from large Pt-Pd nanoparticles in the fresh and 800 °C aged samples. . . . .	52
5.10	HAADF-STEM images showing beam damage in a sample region after EDX mapping of a large Pt-Pd nanoparticle. . . . .	54
5.11	CO oxidation versus temperature curves for the fresh and aged catalyst samples. . . . .	56

## List of Tables

5.1	Summary of the microstructural changes of the catalyst sample due to ageing. . . . .	53
5.2	Results of the BET surface area measurements of the fresh and aged samples. . . . .	54

## List of abbreviations

ADF .....	Annular dark-field
BET method .....	Brunauer-Emmett-Teller method
BF .....	Bright-field
BSE .....	Backscattered electrons
EDX spectroscopy ..	Energy-dispersive X-ray spectroscopy
FIB/SEM .....	Focused ion beam / scanning electron microscopy
HAADF .....	High-angle annular dark-field
HC .....	Hydrocarbons
NO <sub>x</sub> .....	NO and NO <sub>2</sub>
NSR catalyst .....	NO <sub>x</sub> storage and reduction catalyst
PM .....	Particulate matter
PSD .....	Particle size distribution
SCR .....	Selective catalytic reduction
SE .....	Secondary electrons
SEM .....	Scanning electron microscopy
STEM .....	Scanning transmission electron microscopy
TEM .....	Transmission electron microscopy
TWC .....	Three-way catalytic converter
wt.-% .....	weight percent





# 1 Introduction

Air pollution from the transport sector, usually by exhaust from combustion engines, is a major concern for the worldwide climate and air quality, which in turn influences the environment and human health [1–3]. Apart from  $\text{CO}_2$ , which gained a lot of attention for participating in the greenhouse effect, there are several toxic and hazardous components in a typical engine exhaust, the main being carbon monoxide ( $\text{CO}$ ), unburned hydrocarbons, particulate matter and nitrogen oxides ( $\text{NO}_x$ ). Worldwide, regulations are in place to limit the amount of hazardous components emitted from vehicles. The most recent and stringent European emission regulation is called 'Euro 6' and came in place 2014 [4].

Catalytic converters were developed to reduce the vehicle emissions of hazardous components, the first and most used one is the three-way catalytic converter (TWC) [5]. It contains noble metal nanoparticles (consisting of Pt, Pd and/or Rh) dispersed on a porous high surface area support material like  $\gamma$ -alumina, zirconia or ceria and is able to simultaneously oxidise  $\text{CO}$  and hydrocarbons to  $\text{CO}_2$  and  $\text{H}_2\text{O}$ , as well as reduce  $\text{NO}_x$  to  $\text{N}_2$ . For lean-burn and diesel engines, where the TWC cannot be applied successfully, more complex solutions like the  $\text{NO}_x$  storage and reduction (NSR) catalyst [1, 6, 7] need to be used, but the working principal and basic components are very similar.

Degradation of the catalysts (catalyst deactivation) is a major problem when it comes to fulfilling the emission regulations after several years of usage. Common causes for deactivation are thermal effects on the catalytic nanoparticles, like nanoparticle sintering, or the support material, and chemical effects (poisoning) due to substances such as  $\text{SO}_2$  in the exhaust gas [8,9]. One of the most important effects is nanoparticle sintering, which describes particle growth as a result of the catalyst being exposed to elevated temperatures and various gas environments. With the total amount of catalytic material unchanged, the larger nanoparticles expose less surface area for catalytic reaction to occur which yields a activity decrease. Because of deactivation, manufacturers need to design catalytic converters that perform well below the emission limits in many stages of its lifetime. This increases the cost of the catalytic converter and consumption of rare noble metals.

Obtaining an understanding of the microstructural properties and changes that lead to deactivation is crucial when reducing the impact of catalyst ageing on the performance. Special attention is paid to the properties of the noble metal nanoparticles, such as particle size and composition, since they are the ones performing the actual catalytic reactions. Different characterisation methods have been used to

investigate catalytic nanoparticles, among them are gas adsorption / desorption experiments [10–14] (using for example CO which adsorbs selectively to Pt) and X-ray diffraction [15–18].

These methods have in common that they average over large amounts of the catalyst sample, which results in good statistics over many nanoparticles, but at the same time the detailed information about inhomogeneous spatial and size distribution is inaccessible. The most versatile techniques for direct observation of individual nanoparticles include scanning electron microscopy (SEM) and transmission electron microscopy (TEM). While SEM is an appropriate tool to investigate relatively large nanoparticles, TEM is needed to image small nanoparticles, clusters and single atoms of the catalytically active material.

The scope of this work is to explore microstructural changes in a bimetallic Pt-Pd/Al<sub>2</sub>O<sub>3</sub> automotive emission control catalyst induced by ageing treatment, and to link these changes to variations in the observed catalytic activity. Interesting microstructural aspects are nanoparticle size distributions, shapes and chemical compositions. In addition, variations in the particle size distributions as a function of position on the support are of importance. Investigations of fresh and aged catalyst samples were performed using high resolution electron microscopy and spectroscopy, as well as CO oxidation experiments to evaluate their activity. Special effort was made to perform quantitative analyses whenever possible. For this reason, a new TEM specimen preparation method was developed that permits imaging of the catalyst support particles in a cross-section view and extraction of more quantitative information compared to traditional methods.

This thesis is structured in the following way: Chapter 2 describes the basic concepts of heterogeneous catalysis, automotive catalytic converters and catalyst deactivation. In Chapter 3, the catalyst material as well as experimental methods used in this work are introduced. Chapter 4 contains a summary of different TEM specimen preparation techniques that were used, including a detailed description of the FIB/SEM preparation method, and is based on Paper I. The advantages of the FIB/SEM technique are demonstrated by STEM measurements of the obtained specimens. Chapter 5 contains the ageing studies of the catalyst, including SEM, STEM, FIB/SEM and CO oxidation experiments, and is based on the contents of Paper II. Finally, conclusions and an outlook are presented in Chapter 6.

## 2 Heterogeneous catalysis and deactivation

Catalysis describes a phenomenon that increases the rate of a chemical reaction due to the addition of a so-called catalyst. It does so by offering an energetically more favourable reaction pathway compared to the non-catalysed reaction. The catalyst itself is not consumed in the catalytic reaction, so after each reaction cycle it is available to catalyse the next reaction.

Catalysts can have many different forms, ranging from atoms or molecules over small particles to larger structures like enzymes or solid surfaces. They can also have different phases and surroundings and are usually divided into three main categories: Homogeneous catalysts, where the reactants and the catalyst are in the same phase, heterogeneous catalysts, where the catalyst is solid and the reactants gaseous or liquid, and biocatalysis, where enzymes catalyse chemical reactions.

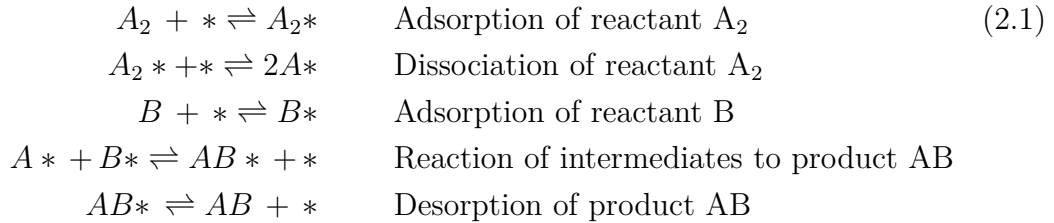
In this work, heterogeneous catalysts for car exhaust aftertreatment will be analysed, so in this chapter these will be introduced in more detail, together with different degradation mechanisms that decrease the activity of heterogeneous catalysts. This is also referred to as catalyst deactivation. Finally, properties of bimetallic Pt-Pd catalysts will be discussed.

### 2.1 Heterogeneous catalysis

In heterogeneous catalysis, the catalyst is usually in the solid phase, whereas the reactants and products of the chemical reaction are in a different phase. In exhaust aftertreatment they are in the gas phase, so this case will be discussed in the following. In a typical catalysed reaction, the reactants adsorb onto the catalyst surface and dissociate if necessary. Then they react on the surface to form a product which desorbs from the catalyst surface, leaving the catalyst unaltered and available for the next reaction.

The catalyst surface can be thought of as consisting of a number of active sites, which are capable of adsorbing the reactants and products. Since a certain number of sites is occupied for each reaction, the total reaction rate on the catalyst surface is limited by the total number of available active sites. A simple catalysed reaction of the reactants  $A_2$  and  $B$  to the product  $AB$  can be expressed in the following

elementary steps (\* denotes an active site and A\* an adsorbed intermediate of species A):



This type of reaction, where all the reactants are adsorbed onto and in thermal equilibrium with the catalyst surface, is called *Langmuir-Hinshelwood* reaction. An important example for this type of reaction in exhaust aftertreatment catalysis is the oxidation of carbon monoxide (CO) to carbon dioxide (CO<sub>2</sub>). A schematic view of this reaction, along with a corresponding energy diagram, is shown in Figure 2.1.

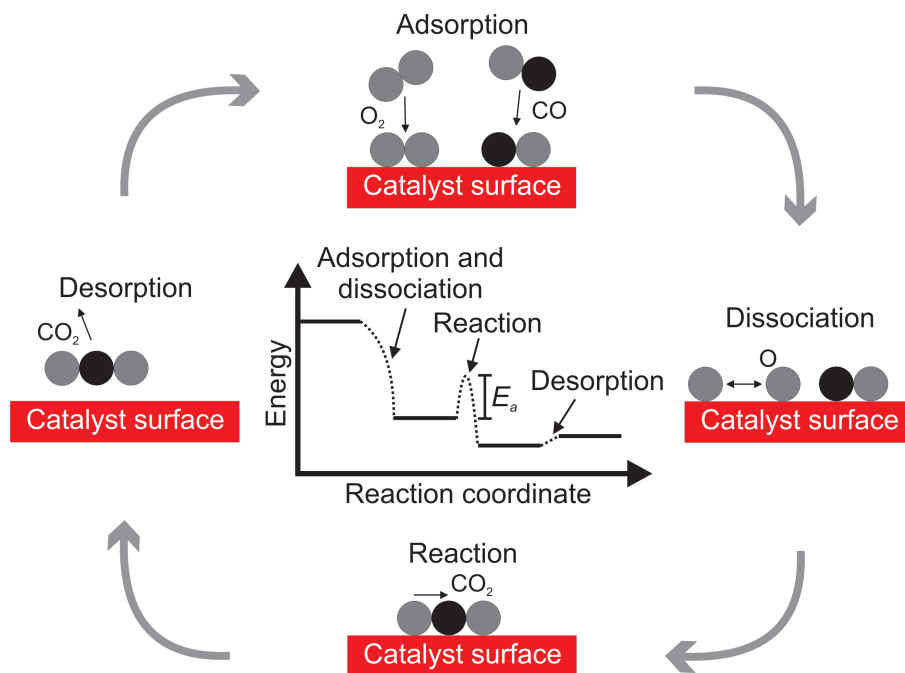


**Figure 2.1:** Schematic of the elementary steps of a catalysed Langmuir-Hinshelwood reaction between CO and O<sub>2</sub> forming CO<sub>2</sub>. As the energy diagram in the center shows, an activation energy  $E_a$  has to be overcome for the reaction to proceed. The activation energy for the catalysed reaction is considerably lower than for the free gas-phase reaction, resulting in a higher reaction rate.

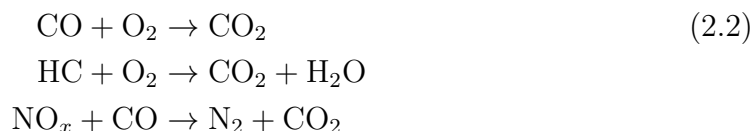
As can be seen in the energy diagram, an activation  $E_a$  is needed for the reaction between CO and O to proceed, whereas no activation energy is associated with the

adsorption of the reactants and the dissociation of oxygen. The activation energy  $E_a$  for the catalysed CO oxidation reaction is around  $50\text{--}100\text{ kJ}\cdot\text{mol}^{-1}$ , whereas in the gas phase an energy of around  $500\text{ kJ}\cdot\text{mol}^{-1}$  is associated with reaction [19]. This demonstrates the main function of the catalyst in this case: It helps by adsorbing and easily splitting the oxygen molecules, which is the most difficult step in the uncatalysed reaction, lowering the overall activation energy for the reaction. In this way, the catalyst increases the reaction rate considerably.

There are several conditions that a catalyst needs to fulfil in order to be suitable for a certain reaction. All the reactants need to adsorb easily onto the catalyst, but no reactant may adsorb so strongly that it covers too much of the surface and inhibits the adsorption of the other reactants (so-called poisoning). Equivalently, the product of the reaction must only be loosely bound to the active sites, otherwise it might not desorb easily enough and poison the catalyst, hindering adsorption of the reactants.

## 2.2 Automotive catalytic converters

In the exhaust aftertreatment system of a petrol engine, three chemical reactions need to occur in order to remove the most hazardous components from the engine exhaust: carbon monoxide needs to be oxidised, different hydrocarbons (HC) need to be oxidised and nitrogen oxides (NO and NO<sub>2</sub>, summarised as NO<sub>x</sub>) need to be reduced. The non-balanced reactions are:



Noble metals, mainly platinum, palladium and rhodium, have proven very effective for these reactions and are used in the so-called *three-way catalytic converter* (TWC), which is the most widespread solution for exhaust aftertreatment in passenger cars today. All of the three reactions mentioned above occur simultaneously in the TWC. For this to be possible, it is important that the air-to-fuel ratio in the exhaust gas composition is held very closely to 14.7:1, the stoichiometric ratio. If the oxygen concentration is higher, too much carbon monoxide will be oxidised, deteriorating the NO<sub>x</sub> reduction. Less oxygen, and the NO<sub>x</sub> will be reduced efficiently, but not all of the carbon monoxide and hydrocarbons will be converted. The correct stoichiometric composition is achieved by using an oxygen sensor, a so-called  $\lambda$ -sensor, that regulates the injection system of the engine.

For a TWC, as for most heterogeneous catalysts, the reactions occur only on the surface, as explained in the previous section. Therefore, in order to use the

expensive noble metals efficiently, the surface-to-volume ratio of the catalyst needs to be maximised. This is usually done by dispersing the noble metals in the form of nanoparticles. An important measure is the dispersion of the noble metal phase, which is the ratio between the number of the surface atoms and the total number of atoms of the noble metal. In many cases, the number of surface atoms correlates with the number of active sites. Another useful measure is the noble metal nanoparticle size, a high dispersion correlates with small metal particles.

The nanoparticles are commonly dispersed onto a support material with a high surface area per volume. The most common support materials in automotive converters include  $\gamma$ -alumina ( $\text{Al}_2\text{O}_3$ ), silica ( $\text{SiO}_2$ ), zirconia ( $\text{ZrO}_2$ ) and ceria ( $\text{CeO}_2$ ). The dispersion of the catalytic material onto the support structure is usually done by wet impregnation: The support material in powder form is soaked in an aqueous solution containing a precursor (salt) of the catalytic element. Electrostatic and capillary forces distribute the salt over the entire surface of the material where they adsorb or ion exchange, given that the precursor salt and pH condition were chosen correctly for the respective support material. Afterwards, the catalyst powder is dried and subsequently calcined at a temperature around 400-500 °C to remove salt residues.

To hold the impregnated support material in place and allow a good gas flow with low pressure drop through the catalytic converter, the catalyst powder is washcoated onto a monolith structure composed of parallel and uniform channels. The monolith can be composed of metals or ceramic materials, most commonly cordierite. The thickness of the washcoat layer is on the order of tens of micrometres. Figure 2.2 shows the structure of a catalytic converter at different length scales.

Although the TWC has had enormous success in improving the exhaust quality of cars over decades, it has severe limitations. As today's car manufacturers push towards the most fuel efficient engines possible [20], lean-burn and especially diesel engines become more and more popular [21, 22]. The exhaust from these engines contains a higher amount of oxygen compared to the stoichiometric air-to-fuel ratio of 14.7:1, typically it lies around 20:1 [19]. As mentioned earlier, a higher oxygen content in the exhaust leads to a decrease in  $\text{NO}_x$  conversion, which means higher  $\text{NO}_x$  emission, when using a TWC. For this reason, the TWC cannot be applied for  $\text{NO}_x$  abatement in combinations with lean-burn and diesel engines.

Due to the strong negative effects of  $\text{NO}_x$  in the atmosphere, including acid rain and the risk of respiratory illnesses [2, 3], in many countries laws are in place to regulate the maximum amount of  $\text{NO}_x$  emission permitted from vehicles. Figure 2.3 shows the development of the European regulations for the emissions of  $\text{NO}_x$  and particulate matter (PM) for diesel passenger between 1992 and 2014, similar regulations are in place for different vehicle types and in different regions of the world. As can be seen, from 1992 to 2014 the maximum amount of  $\text{NO}_x$  emitted from a diesel passenger car was reduced from 970 mg/km to 80 mg/km [4, 23–25].

In order to fulfil these stringent regulations, alternative solutions need to be used

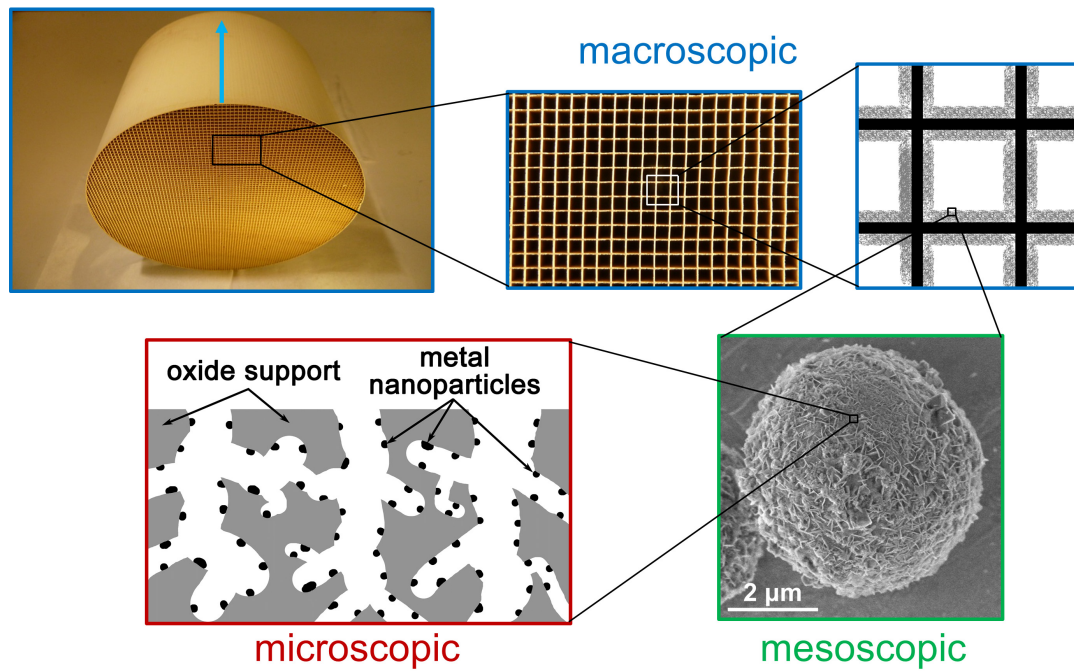


**Figure 2.2:** Structure of an automotive catalytic converter at different length scales: Gas flows through a monolithic channel structure (blue arrow), the channel walls are coated with a washcoat material. The washcoat consists of porous oxide support particles, in which the catalytically active nanoparticles are dispersed.

for  $\text{NO}_x$  abatement in combination with lean-burn and diesel engines. A possible solution for passenger cars is the  $\text{NO}_x$  storage and reduction (NSR) catalyst. The basic idea behind the NSR catalyst is to store the  $\text{NO}_x$  inside the catalytic converter as long as the exhaust conditions don't allow an efficient conversion. This is done by addition of barium oxide ( $\text{BaO}$ ) to the washcoat layer. Under oxidising conditions,  $\text{BaO}$  effectively stores  $\text{NO}_2$  by forming barium nitrate ( $\text{Ba}(\text{NO}_3)_2$ ) on the surface. For this step it is important that the  $\text{NO}$  has been oxidised to  $\text{NO}_2$  before adsorbing on the barium, which happens easily on the noble metal sites. A close proximity of the noble metal sites and the  $\text{BaO}$  is advantageous for this process.

The  $\text{NO}_x$  is stored while the engine is run under lean conditions for several minutes, until a short fuel rich pulse of a few seconds is initiated, under which the exhaust has less oxygen. During this time, components like hydrocarbons,  $\text{CO}$  and  $\text{H}_2$  are able to reduce the stored nitrate species to nitrogen. Again, a close proximity of the stored nitrates to the noble metal sites is beneficial for the reduction reactions. The engine is then switched back to lean mode and a new storage cycle begins. Overall, the engine is still run in lean mode, although the short rich pulses give a small fuel penalty.

An alternative solution that is mainly used for heavy-duty vehicles is selective

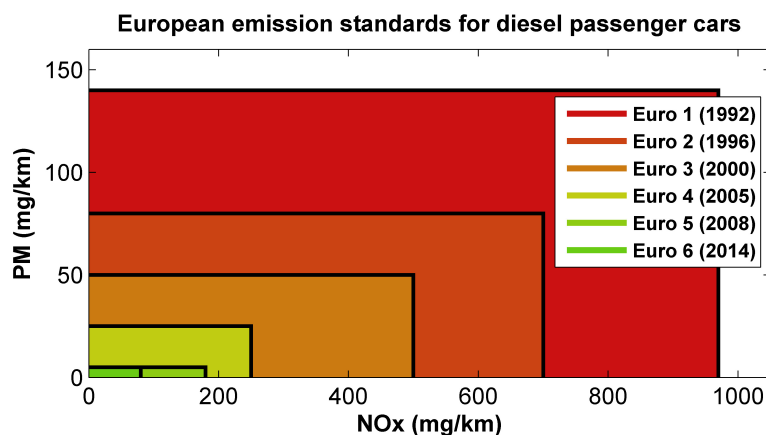


**Figure 2.3:** European emission legislation for diesel passenger cars from 1992 to 2014. Shown are the regulations for NO<sub>x</sub> and particulate matter (PM). Data from references [4, 23–25].

catalytic reduction (SCR), where a reducing agent is added to the exhaust gas in order to selectively react with NO<sub>x</sub> over the catalyst [1].

## 2.3 Catalyst deactivation mechanisms

A catalyst might show very high activity when it is freshly produced, but over time different deactivation mechanisms will deteriorate its performance, which is a major problem. In the case of the European emission standard 'Euro 6', a passenger car needs to fulfil the emission limits after 100 000 km or five years of use [4]. This means that the fresh catalyst needs to be designed to a much higher activity at first, resulting in higher consumption of expensive noble metals like platinum, palladium and rhodium. Catalyst deactivation is usually linked to the loss of active sites for the chemical reactions due to high-temperature exposure or contact with chemical species in the exhaust gas. The main deactivation mechanisms will be introduced here.

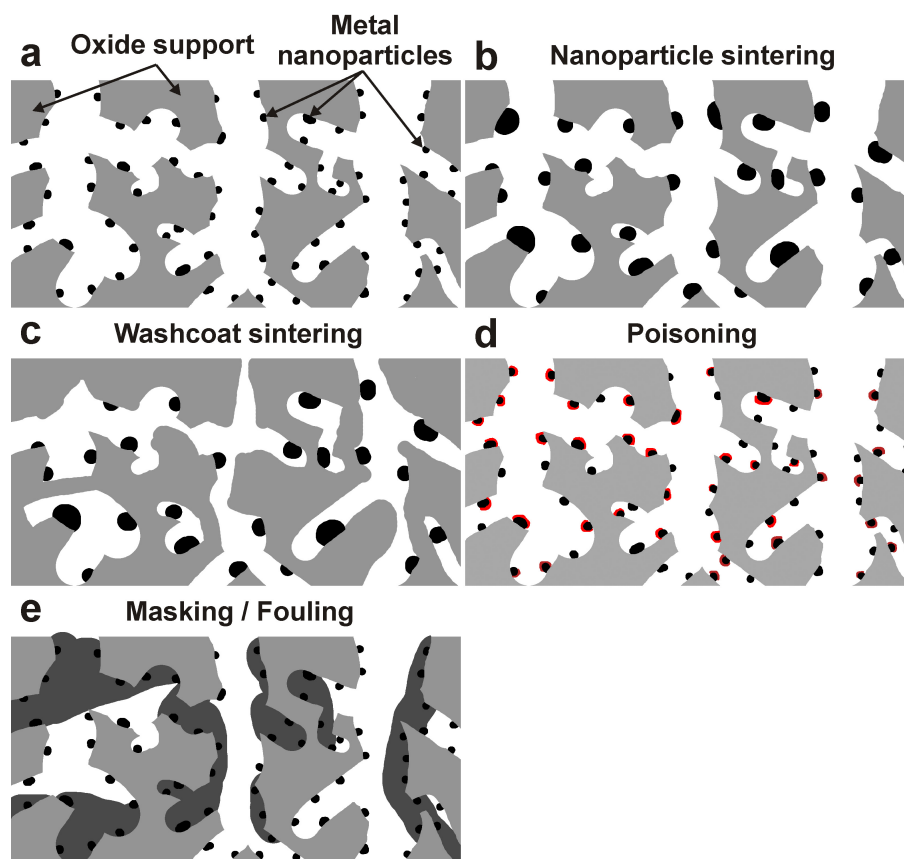
### Nanoparticle sintering

Figure 2.4a shows the typical structure of a fresh catalyst with small, well dispersed metal nanoparticles inside a porous support material. The main cause of thermal deactivation is sintering of the metal nanoparticles. Under the influence of heat, the size of the nanoparticles will increase, which decreases the surface-to-volume ratio of the catalytic material.

As mentioned in Section 2.2, the chemical reactions occur only on the surface, so particle sintering will usually decrease the catalytic activity. The driving force



for this process is the reduction of surface energy and number of under-coordinated atoms. The temperature at which particle sintering occurs and the degree of sintering vary depending on materials [26] and gas environments, water vapour is believed to promote the sintering process [27–30]. The sintering onset temperature lies usually well within the temperature range the catalyst is exposed to during normal usage.



**Figure 2.4:** Schematic view of different catalyst deactivation mechanisms. a) The catalyst in the fresh state, with small dispersed metal nanoparticles on the porous oxide support. b) Nanoparticle sintering leads to larger nanoparticles with a lower total surface area. c) Washcoat sintering: At high temperatures the washcoat material can sinter, leading to blocked pores and a lower total accessible surface area. d) Poisoning: Chemical substances can selectively block active sites by adsorption or chemical reactions. e) Masking / Fouling: Contaminations (e.g. carbon) can non-selectively adsorb to the sample and block access to the active sites.

Figure 2.4b shows the catalyst with enlarged, sintered nanoparticles. There are two different mechanisms of particle sintering, namely particle migration and coalescence, where entire nanoparticles migrate over the support, and atomic migration, where individual atoms migrate from smaller to larger nanoparticles via diffusion

on the support or vapour phase transport. Several studies have been performed to investigate which of these mechanisms is the dominant in different situations, both on flat model systems [31–33] and on more complex structures [32,34,35]. Although conclusions about the sintering mechanism could be drawn in some cases, a general prediction for the behaviour of other systems and conditions seems to be difficult. It has been suggested that particle migration plays a role during the initial stages of sintering, while atomic migration is dominant during later stages [36].

Nanoparticle sintering was also observed in other studies which included catalytic activity measurements [29], sintering on different support materials [37] or chemical effects [38]. Most studies suggest an onset for severe platinum nanoparticle sintering on  $\gamma$ -alumina in oxidising environments at about 550–600 °C [27,39].

### Support sintering

Another possible thermal deactivation mechanism is sintering of the catalyst support structure. The pore structure of the support can change, resulting in total or partial blockage of some pores, making active sites inside these pores unavailable or increasing the pore diffusion resistance for the gas. Figure 2.4c shows a schematic image of a catalyst after pore (and nanoparticle) sintering. Sintering of the support material usually requires higher temperatures than nanoparticle sintering. A second mechanism of support sintering involves a change in the crystal structure of the support material, which normally induces a loss of total surface area and encapsulation of active sites.

In case of the most common support material,  $\gamma$ -alumina, the first phase transformation occurs around 800 °C to  $\delta$ -alumina, then at about 1000 °C to  $\theta$ -alumina and finally at around 1100 °C to  $\alpha$ -alumina, the most stable phase with only about 2% of the original surface area [1]. Heating to temperatures close to 1100 °C therefore has to be avoided under all circumstances. For certain support materials, adding stabilisers like  $\text{La}_2\text{O}_3$  can help to reduce the rate of support sintering.

### Poisoning

Poisoning is a chemical deactivation mechanism. It describes a process where a chemical component in the gas phase interacts with the catalyst and decreases its activity. Some poisons like lead can chemically react with the metallic nanoparticles, forming an inactive alloy, while others like  $\text{SO}_2$  only chemisorb onto the nanoparticles, blocking active sites on the surface and thereby decreasing the activity [1]. The latter process can be reversible in some cases. Desulfation of a catalyst is usually carried out at high temperatures, above 600 °C, under rich conditions, where CO and  $\text{H}_2$  can reduce sulfate species formed under lean conditions [6]. Additionally, the support material can be modified to improve  $\text{SO}_2$ -poisoning resistance [40]. Figure 2.4d shows a situation where the catalytic nanoparticles are partly covered

by an adsorbed poison. Another possible mechanism is the reaction of the support material with a poison, which can result in partial pore blocking.

### Masking/Fouling

Masking or fouling is a deactivation mechanism similar to poisoning, but does not specifically affect certain components. Instead, contamination, often carbon, physically covers parts of the pore structure and the catalytic nanoparticles, thereby hindering the exhaust gas to reach those active sites. Figure 2.4e shows an illustration of a masked catalyst.

### Gas-solid and solid-state reactions

Apart from the reactions of gas phase components with the catalyst to form inactive products as mentioned in the paragraph 'Poisoning', gas phase species can also react with catalytic components, form volatile compounds and leave the catalyst, resulting in a loss of catalytic material [8]. Also solid-state reactions between different components of the catalyst can deteriorate its performance, one example being the formation of  $\text{BaAl}_2\text{O}_4$  during vehicle ageing of a  $\text{BaO}/\text{Al}_2\text{O}_3$  based NSR catalyst [41].

## 2.4 Bimetallic Pt-Pd catalysts

Usually, more than one catalytic component is used in automotive catalytic converters. A popular choice is the addition of Pd to a Pt catalyst, often in small amounts as an additive. Several reasons could motivate such a decision, either the properties of the bimetallic catalyst could be better than both of the pure systems, the price of the catalyst could be reduced by adding a cheaper component while using less of the more expensive one, or both of these possibilities. Several studies have addressed the properties of bimetallic Pt-Pd catalysts.

It was generally observed that Pt-Pd catalysts show a lower degree of nanoparticle sintering compared to corresponding monometallic Pt or Pd catalysts, the addition of Pd seems to have a stabilising effect on the nanoparticles [39, 42–44]. Studies of the catalytic activity for CO and hydrocarbon oxidation show a slightly better performance of the Pt-Pd system [45] and less degradation of the activity after ageing [42, 46].

An interesting aspect of bimetallic catalysts is the degree of alloying between the two components. The nanoparticles could be monometallic in themselves with the two different particles (pure Pt and Pd) randomly distributed over the support, or the two metals could be alloyed to form Pt-Pd nanoparticles. In case of alloyed nanoparticles, two of the possible structures are homogeneous alloys and

core-shell structures. In a core-shell nanoparticle, usually the component with the lower surface energy would form the shell of the nanoparticle.

Morlang et al. [42] studied the oxidation state of Pd and the degree of alloying of a Pt-Pd catalyst after ageing under oxidising conditions. They found that the Pd was partly in a metallic state even after the ageing, but that the PdO was present in the form of separate nanocrystals instead of a PdO shell around the Pt particles. Ezekoye et al. [43] also investigated alloying between Pt and Pd and found that after ageing at high temperatures the degree of alloying between the two elements was high, independent of the initial distribution.

Ward et al. [47] investigated a commercial Pt-Pd catalyst and found random alloying in the untreated samples, whereas vehicle-ageing induced surface segregation of Pd only in a minority of the nanoparticles. Johns et al. [48] studied an aged Pt-Pd catalyst and found an uneven distribution of Pt and Pd, where the larger nanoparticles were rich in Pt, whereas the more dispersed phase was rich in Pd.

## 3 Materials and methods

In this chapter, the catalytic material and the experimental methods used for this thesis will be described. The experimental methods include routinely used methods like surface area measurement of the catalytic material by N<sub>2</sub> physisorption, the hydrothermal ageing procedure and the protocol for catalytic activity evaluation by CO oxidation experiments. Additionally, catalyst characterisation by electron microscopy (scanning electron microscopy (SEM), focused ion beam / scanning electron microscopy (FIB/SEM) and scanning transmission electron microscopy (STEM)) will be described, including X-ray spectroscopy and the procedure of obtaining particle size distributions from the microscopy images.

### 3.1 Catalyst sample

In this study, a commercially produced bimetallic Pt-Pd catalyst supported on  $\gamma$ -alumina was investigated. The same Pt-Pd concentrations and preparation method (based on wet impregnation) as for a commercial NSR catalyst were used, but the NO<sub>x</sub> storage component was not added to this test sample in order to reduce the complexity and enable systematic studies of the nanoparticle sintering behaviour. The noble metal loadings for this catalyst are 0.17 wt.-% platinum and 0.03 wt.-% palladium, corresponding to an atomic Pt:Pd ratio of 3.1:1.

The catalyst sample was received in powder form, containing the impregnated alumina support agglomerates, which in turn are built up by small primary  $\gamma$ -alumina particles. The density of the powder sample was measured to about 0.6 g/cm<sup>3</sup>. The alumina agglomerates, in the following called 'alumina support particles', are typically in the size range of a few hundred nanometres to several micrometres.

### 3.2 Hydrothermal ageing

To simulate the conditions that the catalyst might be exposed to during its lifetime in a catalytic converter of a vehicle, the sample was exposed to hydrothermal ageing in a gas flow reactor at different temperatures. The gas flow reactor consists of a quartz tube containing the sample, which is surrounded by a metal coil for resistive heating. The tube can be sealed and gas with a defined composition can be fed through, controlled by mass flow controllers. Thermocouples are introduced into

the sample to determine its temperature, the readout is used as feedback to the heating power supply in order to maintain the desired temperature.

For the hydrothermal ageing, the catalyst powder was loaded into a modified ceramic monolith (usually used for holding the washcoat layer as explained in Section 2.2) which was cut from one side to create an opening, while still allowing a reasonable gas flow around and through the powder. The total gas flow in the reactor did not exceed 1 L/min in order to keep the powder in place. Ageing was performed at 500 °C, 600 °C, 700 °C and 800 °C. The sample was heated up in pure argon at a rate of 7 °C/min. After that, it was exposed to an atmosphere of 75 vol.-% argon, 15 vol.-% oxygen and 10 vol.-% water vapour for 24 hours. Cooling was done in pure argon for at least two hours before the powder was removed from the reactor. Figure 3.1 shows the monolith filled with catalyst powder in the reactor tube and the reactor during ageing.

It should be noted that this synthetic ageing protocol does not simulate all aspects of real engine ageing in a vehicle. Although some key aspects like the oxidising environment (which is true most of the time in a real exhaust) and the presence of water vapour are reproduced, engine exhausts contain a variety of complex components [1] which can influence the ageing process. Also, the temperature profile can be different and more dynamic than in this simulated ageing. Despite these differences, studies have shown that synthetic ageing can reproduce many aspects of real vehicle ageing, especially when thermal effects on nanoparticle stability and sintering are the main concern [49].

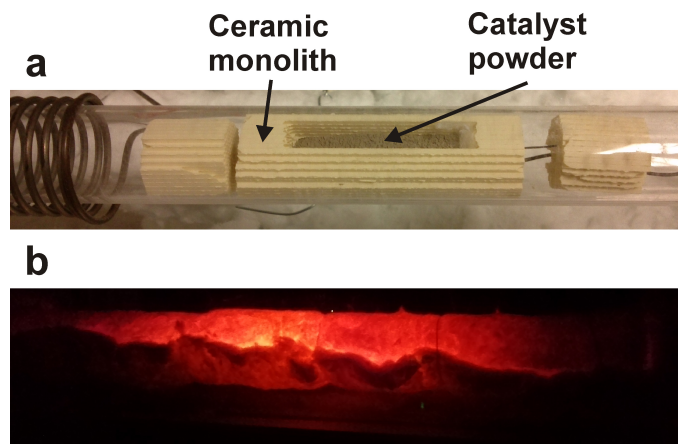


**Figure 3.1:** a) Image of the modified monolith, filled with catalyst powder, in the reactor tube. The heating coil seen to the left covers the whole area during ageing. b) Image of the reactor during ageing at 800 °C.

### 3.3 Surface area measurements (BET method)

The total surface area of the catalyst samples was determined by nitrogen physisorption at liquid nitrogen temperature followed by an evaluation after the Brunauer-Emmett-Teller (BET) method. Nitrogen was adsorbed onto the sample while the total adsorbed volumetric quantity of nitrogen  $\nu$  and the corresponding nitrogen partial pressure  $p$  were measured. Assuming layer-wise adsorption and no interaction between the layers, the BET equation is [1]:

$$\frac{p}{\nu \cdot (p_0 - p)} = \frac{c - 1}{\nu_m c} \left( \frac{p}{p_0} \right) + \frac{1}{\nu_m c} \quad (3.1)$$

with

$$c = e^{\frac{H_1 - H_L}{RT}} \quad (3.2)$$

where  $p_0$  is the saturation pressure at the used temperature,  $c$  is the BET constant,  $\nu_m$  is the volume adsorbed at monolayer coverage,  $H_1$  is the heat of adsorption of the first and  $H_L$  of the following monolayers,  $R$  the gas constant and  $T$  the temperature.

If the left side of equation 3.1 is plotted against  $p/p_0$ , a linear plot is obtained. The assumption of such linear behaviour is usually valid in the range of  $0.05 < p/p_0 < 0.3$ . The slope  $a$  and y-intersect  $b$  of the curve can be measured in that range and the monolayer adsorbed gas quantity  $\nu_m$  can be calculated:

$$\nu_m = \frac{1}{a + b} \quad (3.3)$$

Now, the BET surface area can be calculated:

$$S_{BET} = \frac{\nu_m N s}{V M} \quad (3.4)$$

where  $N$  is Avogadro's number,  $s$  the adsorption cross section of a nitrogen molecule,  $V$  the molar volume of nitrogen and  $M$  the total mass of the catalyst sample. The measurements in this work were performed using a Micromeritics Tristar<sup>TM</sup>. Prior to the experiment, the specimens were degassed in vacuum.

### 3.4 Catalytic activity evaluation: CO oxidation

The catalytic activity of the fresh and aged samples was determined by CO oxidation experiments. The catalysts were coated onto ceramic monoliths by dip-coating

using a washcoat slurry composition of 80 % water, 16 % catalyst powder and 4 % böhmite. The monoliths were exposed to a heating gun for short times for drying and transforming the böhmite to alumina. A total amount of 200 mg washcoat (after drying) was used for each monolith. Afterwards, the monoliths were calcined in an oven at 500 °C for 60 minutes to stabilise the washcoat layer, improve the adhesion to the monolith and remove contaminations.

The monoliths were then inserted into a gas flow reactor similar to the one used for hydrothermal ageing (Section 3.2). The inlet gas to the reactor was controlled by gas flow controllers, heating was performed by resistive heating of a metal coil around the quartz tube, and the sample temperature was measured by thermocouples inserted into a central channel of the monolith. The outlet gas was analysed by a quadrupole mass spectrometer (Pfeiffer Prisma<sup>TM</sup>). During the experiments the reactor was insulated using glass wool to reduce heat losses and ensure an even temperature profile within the sample region.

Prior to the CO oxidation experiments, the samples were heated up in pure argon to 450 °C using a heating rate of 5 °C/min and a total gas flow of 500 ml/min. 4 vol.-% oxygen were added to the stream for 10 minutes to obtain a defined initial oxidation state for all samples. After that, 1000 ppm CO and 4 vol.-% oxygen balanced with argon (total flow: 500 ml/min) were introduced into the reactor, and the outlet CO and CO<sub>2</sub> concentrations were determined using the mass spectrometer. The CO-to-CO<sub>2</sub> conversion was calculated using the inlet CO and outlet CO<sub>2</sub> concentrations.

The temperature was then reduced to 50 °C and again increased to 450 °C two times, resulting in CO conversion measurements during two heating and two cooling ramps. Due to the possibly different oxidation and CO poisoning states at the beginning of the heating and cooling ramps, the conversion curves are usually slightly shifted with respect to each other (hysteresis-like behaviour).

## 3.5 Scanning electron microscopy (SEM)

Scanning electron microscopy (SEM) was used in this study to image the oxide support particles as well as large Pt-Pd nanoparticles (larger than 10 nm) and perform chemical analysis by means of X-ray spectroscopy. The following short description of the technique is based on a book by Goldstein et al. [50]. In an SEM, electrons are emitted from an electron source, usually a field-emission gun, and then accelerated by a high voltage. Typical electron energies are 0.1-30 keV. The electrons enter a system of two or more electromagnetic lenses which form an electron beam focused to a small spot, representing a demagnified image of the tip of the electron gun.

The surface of the specimen is placed in the plane of the cross-over of the focused electron beam. The electrons enter the specimen and interact through elastic and inelastic scattering in the so-called interaction volume, which can have dimensions



up to several micrometres, depending on the acceleration voltage. Different signals are created inside the specimen, and the depth from which they can escape the specimen and be detected depends on their mean free path inside the specimen material. The electron beam is then rastered across the specimen surface using scan coils and the different signals, that are generated from the interaction between the specimen and the electron beam, can be recorded for each beam position, resulting in a two-dimensional representation of the specimen.

Secondary electrons (SEs) are created by inelastic scattering of the electron beam which ionise atoms in the material. The SEs have low energies, typically below 10 eV. With these low energies, the SEs are easily reabsorbed by the material, leading to a very localised SE emission close to the incident electron beam (within a few nanometres). SEs are usually used to obtain topographic information about the specimen, since the probability of SE emission is higher close to edges where the electrons can escape in more directions compared to a flat surface.

Backscattered electrons (BSEs) are created by elastic scattering of the incident electrons, so their energies are close the energy of the incident beam. The BSEs have a larger mean free path up to 100 nm (depending on their energy) and can therefore be created further away from the incident beam. BSEs can be used to obtain images with compositional contrast because the probability for elastic scattering increases with the atomic number,  $Z$ , of the atoms in the material. Regions with heavier atoms therefore create more BSEs, leading to a higher intensity in the final image compared to a region with lighter atoms. BSEs can also created SEs at positions further away from the incident beam compared to the direct SE signal, but these SEs contribute mainly to a smooth background signal.

Characteristic X-rays constitute the third important signal in the SEM. They are created by radiative relaxation of atoms in the material, where electrons relax to a lower energy state of more inner electron shells. The energies of the X-rays can be analysed and used to identify and quantify elements present in the specimen. The process of acquiring and evaluating X-ray spectra will be described in more detail in Section 3.8.

Figure 3.2 summarises the different signals and detectors most frequently used in SEM. The SEM results presented in this thesis were obtained using a Zeiss Ultra-55<sup>TM</sup> SEM operated at an acceleration voltage of 10 kV. A backscattered electron detector was used to obtain a clear image contrast of the Pt-Pd nanoparticles within the alumina support. The X-Ray spectra were acquired using a diode-type Si EDX detector (see Section 3.8).

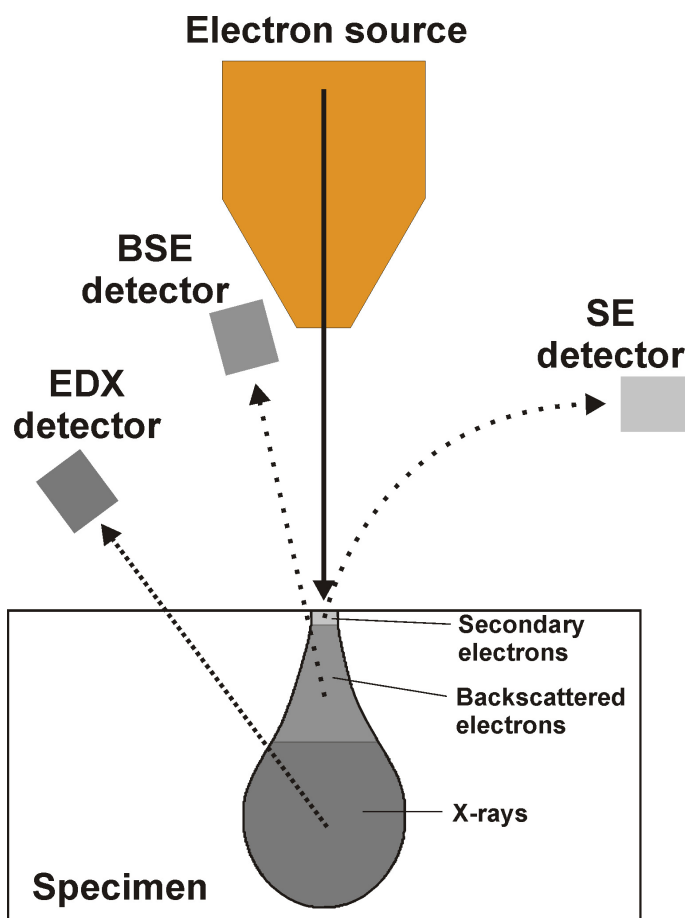


**Figure 3.2:** Schematic drawing showing the different signals commonly used in SEM. SEs are only detected if they are created within a few nanometres from the surface, whereas BSEs and X-rays can originate from a larger depth within the pear-shaped interaction volume.

## 3.6 Scanning transmission electron microscopy (STEM)

### 3.6.1 Imaging principle

For high-resolution imaging of the Pt-Pd nanoparticles and chemical analysis using X-ray spectroscopy, scanning transmission electron microscopy (STEM) was used. STEM is an imaging mode that can be performed in many commercial transmission electron microscopes (TEMs). A TEM uses an electron source and electron optics in front of the specimen similar to those in an SEM, but the typical range of acceleration voltages is 60-300 kV. In contrast to the conventional TEM imaging mode, in which the microscope works similarly to a conventional light microscope

and electromagnetic lenses below the specimen are responsible to create an optical electron image (see reference [51]), the electron beam is focused to create a small cross-over in the plane of the specimen like in the SEM when operating in STEM mode.

The electron beam then scans over the specimen, but instead of using the SEs or BSEs like in the SEM, the transmitted electrons are used in STEM mode to form an image. This implies that the specimen has to be very thin, from 10 nm to a few hundred nanometres, depending on the material and desired resolution and contrast. The incident electrons can either pass through the specimen without interaction or they can scatter elastically or inelastically. Electrons which are not scattered or scattered to small angles can be detected by a small detector positioned on the optical axis. If these electrons are used, bright-field (BF) imaging is performed. In BF mode, the image shows mainly phase contrast like in conventional TEM imaging [52]. If a concentric annular detector is used, which excludes those electrons close to the optical axis, annular dark-field (ADF) imaging is performed.

If the inner acceptance angle of the electron detector is larger than about 40 mrad, this technique is called high-angle annular dark-field (HAADF) imaging. Figure 3.3 shows a schematic overview of the incoming electron beam on the specimen and the different signals that can be used. When using such large scattering angles, most of the scattering occurs very close to the nucleus of the scattering atoms, changing the  $Z$ -dependence ( $Z$ : atomic number of scattering atoms) of the scattering cross-section compared to BF or ADF imaging. In HAADF, the scattering is similar to unscreened Rutherford scattering, which has a  $Z^2$  dependence of the scattering cross section. Due to screening by the electron cloud, the practical  $Z$ -dependence varies between  $Z^{1.6}$  and  $Z^{1.9}$  [53].

This means that an atom which has twice the atomic number of another atom scatters (nearly) four times as many electrons to high angles. The image contrast with respect to the chemical composition of the specimen is thus strongly enhanced by this effect. HAADF imaging is therefore often called  $Z$ -contrast imaging. It can also be shown that HAADF imaging is characterised by many incoherent scattering characteristics, thereby minimising the image contrast mechanisms arising from Bragg scattering and interference [52]. This is especially useful when imaging small high density nanoparticles supported on a low density but thicker material. In conventional coherent imaging, interference effects from the support material would obscure the signal from the nanoparticles. In the HAADF mode, the coherent phase interference effects are suppressed and the nanoparticles generate a good signal due to the strong  $Z$ -dependence of the scattering. As the name suggests, HAADF-STEM is a dark field mode. Since electrons scattered to high angles are detected, an image point is brighter the more scattering is caused by the specimen at that position. A hole in the specimen, which does not scatter any electrons at all, will therefore be black in an HAADF-STEM image, whereas thick or dense regions will be bright.

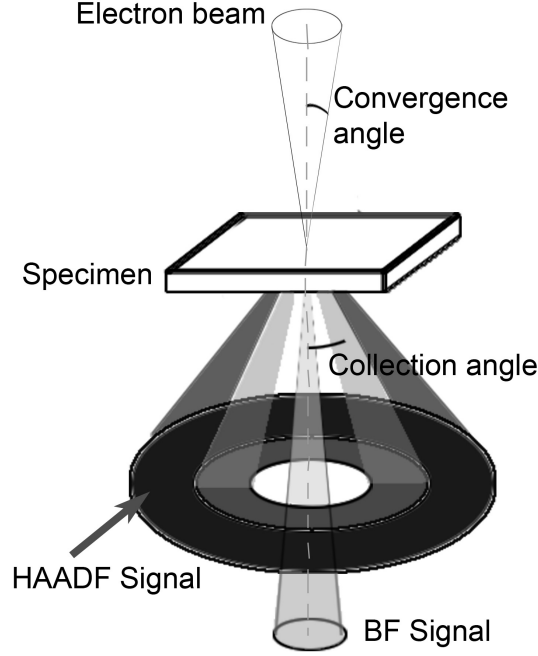


**Figure 3.3:** Schematic drawing showing the convergent electron beam hitting the specimen and the different signals that can be used for STEM imaging. The beam convergence angle is exaggerated here. BF: bright-field, HAADF: high-angle annular dark-field.

### 3.6.2 Resolution and aberrations

The spatial resolution in STEM imaging is mainly limited by the achievable diameter of the focused electron beam on the specimen. The Rayleigh criterion [51] can be used to approximate the beam diameter  $d_b$  and hence the best achievable resolution in STEM, assuming the beam diameter is only diffraction-limited:

$$d_b = 1.22 \frac{\lambda}{\sin(\alpha)} \quad (3.5)$$

where  $\lambda$  is the wavelength of the electrons and  $\alpha$  the convergence semi-angle of the focused electron beam. The convergence semi-angle is mainly determined by the size of the beam limiting aperture above the specimen. The wavelength  $\lambda$  can be calculated using:

$$\lambda = \frac{h}{\sqrt{2m_0eV \left(1 + \frac{eV}{2m_0c^2}\right)}} \quad (3.6)$$

where  $h$  is Plank's constant,  $m_0$  the electron rest mass,  $e$  the electron charge,  $V$  the acceleration voltage of the microscope and  $c$  the speed of light. For a 300 kV TEM, the electron wavelength is around 2 pm. Assuming a convergence semi-angle of 19 mrad (typically used in this work), the approximated theoretical beam diameter and resolution limit is:  $d_b \approx 0.13$  nm.

This resolution, however, can often not be achieved in reality due to the imperfection of the magnetic lenses used in the TEM. Magnetic lenses have many different aberrations, but the ones mainly limiting the resolution in modern (S)TEMs are astigmatism, spherical aberration and chromatic aberration. Besides these, diffraction limits the resolution and was already taken into account when calculating the beam diameter using the Rayleigh criterion above. Astigmatism results from non-uniform (not perfectly cylindrical) magnetic fields in the lenses and leads to an elongation of the focused spot in a certain direction. Stigmators, which are octupoles that create a compensating field, can be used to relatively easy eliminate the effects of astigmatism.

Spherical aberration depicts the effect that off-axis electrons are bent stronger towards the optical axis compared to electrons travelling closer to the optical axis. A point object is imaged as a disc as a result of this aberration, leading to a degraded resolution. In the focal plane, the diameter of the disc caused by spherical aberration can be approximated by [51]:

$$d_{sph} \approx C_s \alpha^3 \quad (3.7)$$

where  $C_s$  is called the spherical aberration coefficient of the magnetic lens. Since there is a very strong dependence on the semi-convergence angle of the electron beam, spherical aberration becomes dominant if too large beam limiting apertures are used. Since decreasing the aperture size leads to less spherical aberration but more diffraction effects, there is an optimum aperture size or convergence angle to balance these two effects. The beam diameter when combining diffraction and spherical aberration can be approximated as [51]:

$$d_b \approx \sqrt{\left(\frac{\lambda}{\sin(\alpha)}\right)^2 + (C_s \alpha^3)^2} \quad (3.8)$$

leading to an optimum semi-convergence angle of  $\alpha_{opt} \approx 0.77 \alpha^{1/4} / C_s^{1/4}$  (from reference [51]).

Since no concave magnetic lenses exist, the correction for spherical aberration is rather difficult but can be performed using complex arrangements of quadrupoles, hexapoles and/or octupoles, so-called spherical aberration or  $C_s$  correctors [54]. A simpler approach to minimize the effect of spherical aberration is to use small

apertures that exclude electrons travelling further away from the optical axis and thereby decrease the beam convergence angle  $\alpha$ . However, this approach also limits the resolution due to diffraction at the aperture, a point object will be imaged as an Airy disc. The use of a  $C_s$  corrector allows the use of larger beam limiting apertures, resulting in a decreased influence of the diffraction effect.

Another important aberration is chromatic aberration, described by the coefficient  $C_c$ . The electron source of a TEM does not emit monochromatic electrons. The energy spread depends on the type of electron source and is on the order of 0.7 eV for a Schottky field emitter [51]. Due to the chromatic aberration not all of the electrons are focused in the same image plane by the lenses, resulting in an increased disc diameter of the electron probe on the specimen. One way to circumvent this problem is to use a monochromator which reduces the energy spread in the beam. Since the beam intensity is reduced considerably by the monochromator, it is often not a good solution when using the imaging mode. A better solution would be lens elements that correct for the effects of chromatic aberration. Those are in development but not yet readily available.

#### 3.6.3 Electron beam damage

Damage induced in the specimen by the electron beam can in some cases limit the possibilities to investigate the intrinsic specimen properties more than, e.g., limited resolution due to lens aberrations. The beam damage is caused by inelastic collisions of the electrons with atoms in the specimen. Beam damage can be divided into three categories which will be introduced here, the influence of beam damage to the different investigations presented later will be discussed in the respective sections. More information about these beam damage mechanisms can be found in reference [51].

##### Radiolysis

The beam electrons can break bonds in some materials through ionisation. Most commonly this happens in polymers, where the electrons can either break the main polymer chains and change their structure and properties, or break side groups and create radicals, which then can form new structures through cross-linking.

##### Knock-on damage / sputtering

Knock-on damage describes the effect of displacement of atoms in the specimen due to the transfer of kinetic energy from the incoming electrons. This can happen in crystalline materials to create point defects, but also in unordered structures. Atoms can also be ejected from the specimen surface, this process is called sputtering. Both of these processes occur if the kinetic energy that can be transferred from the

electrons to the specimen is higher than the threshold energies for displacement and sputtering, which are individual for each element. The maximum kinetic energy that can be transferred depends on the electron energy and is higher for higher energies. With a 300 keV beam, sputtering can be induced in many materials [51].

### Specimen heating

The third beam damage mechanism is specimen heating. It is caused by excited phonons that heat up the specimen, which in turn can change its structure. Heating is only relevant for specimens with poor thermal conductivity, like for example polymers and ceramics. The effect of specimen heating is usually reduced if the energy of the electron beam is increased, as this decreases the cross section for inelastic scattering.

### 3.6.4 Instrumentation

The STEM measurements presented in this thesis were performed using an FEI Titan 80-300<sup>TM</sup> (S)TEM equipped with a Schottky field-emission source operated at an acceleration voltage of 300 kV. The instrument is fitted with a probe aberration corrector which allows focusing the electron probe to a spot smaller than 0.2 nm in STEM mode. All measurements were performed in STEM mode using a HAADF detector for Z-contrast imaging. Inner / outer collection angles between 50 / 250 mrad and 70 / 350 mrad were used. A diode-type Si EDX detector was used to acquire X-ray spectra for chemical characterisation, for more details see Section 3.8. Prior to all TEM investigations, the specimens were cleaned in a diluted oxygen plasma to minimise carbon contaminations.

## 3.7 Particle size analysis

Particle sizes were determined from the SEM and STEM images using the procedure illustrated in Figure 3.4: The raw image (as shown in Figure 3.4a) was analysed and the Pt-Pd nanoparticles were manually identified. Using the software ImageJ [55], the nanoparticles were marked to create a binary image as shown in Figure 3.4b. Using a particle analysis function, all particles in the binary image were detected and their projected area  $A_p$  was measured. Assuming spherical shapes of the nanoparticles, a projected area diameter was calculated using:

$$D_p = 2\sqrt{\frac{A_p}{\pi}} \quad (3.9)$$

The diameters were sorted into equally sized bins and plotted as particle size distributions (PSDs) as shown in Figure 3.4c. Data from many similar images were combined to obtain a statistically relevant amount of particles.

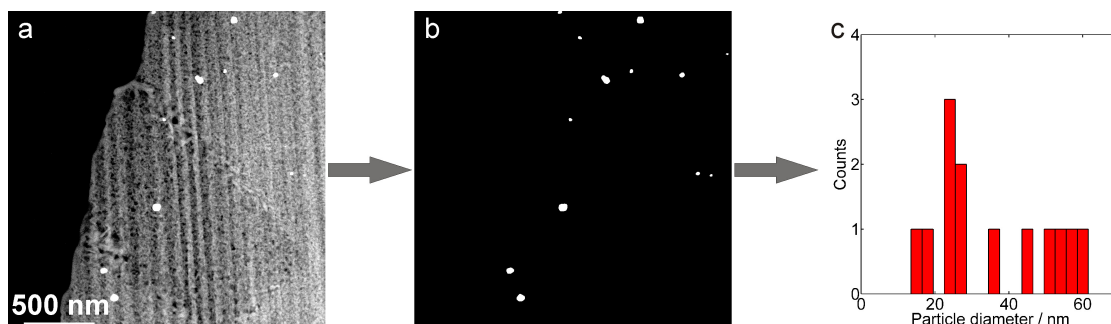


**Figure 3.4:** Process of creating PSDs from SEM and TEM images. Nanoparticles in the image are manually detected and the image is binarised. The projected area of each particle is measured and projected area diameters are calculated. These are sorted into equally sized bins and plotted as a PSD.

## 3.8 Energy-dispersive X-ray (EDX) spectroscopy

The electron beam interaction with the specimen (in either SEM or TEM) creates characteristic X-ray radiation. The incoming electrons ionize part of the atoms in the specimen, electrons from higher electronic states are transferred to lower energy states and the energy difference is emitted as X-ray quanta. Additionally, a continuous background spectrum (Bremsstrahlung) is emitted due to electrons being retarded by electrostatic interactions with the nuclei in the material.

An X-ray detector is mounted above the specimen. The most common type is a solid state Si detector consisting of a reverse-biased p-i-n diode ('p-doped'- 'intrinsic'- 'n-doped'). An X-ray entering the detector creates a number of electron-hole pairs proportional to its energy. The number of separated charges is counted and the energy of the incident X-ray is calculated. The energy resolution of such an energy-dispersive X-ray detector is quite poor, typically around 140 eV [51].

In many cases, the elements present in the specimen can directly be determined from the X-ray lines identified in the spectrum. To quantify the concentrations of different elements, the following procedure can be applied: First, the continuous background in the spectrum needs to be subtracted. One way to do this is to define background windows in regions without characteristic peaks and then model the background in the remaining regions by polynomial functions or by interpolation. Once the background is subtracted, the intensities of a certain family of X-ray peaks (K, L, M, ...) of an element are integrated. If two elements A and B are present



in the specimen and the integrated intensities  $I_A$  and  $I_B$  are measured, the *Cliff-Lorimer* equation allows the calculation of the ratio of the weight percent of each element,  $C_A$  and  $C_B$  [51]:

$$\frac{C_A}{C_B} = k_{AB} \frac{I_A}{I_B} \quad (3.10)$$

$k_{AB}$  is a sensitivity factor that accounts for the difference between the generated and measured X-ray intensities. It depends mainly on the atomic number  $Z$  of the two elements, the absorption of X-rays within the specimen and the fluorescence of X-rays in the specimen. A precise knowledge of this so-called  $k$ -factor is crucial for an accurate quantification, but is in reality often very hard to obtain. The above mentioned steps can be performed almost automatically in most modern EDX software packages.

Pre-defined  $k$ -factors can be used, which often assume that the specimen is thin enough to ignore absorption and fluorescence effects. This simple and automatic approach is often sufficient to obtain useful information about the specimen, estimate chemical compositions and compare different regions of the specimen. One should keep in mind, though, that for a very precise absolute quantification a more thorough determination of the  $k$ -factors is needed, procedures for that are described in reference [51].

Different modes can be used to acquire EDX data. The simplest way is to position the electron beam on one spot of the specimen and acquire a spectrum (spot analysis). Alternatively, the electron beam can be scanned continuously over an area of the specimen while a spectrum is collected. This spectrum will then show the integrated (average) composition of that region. If spatially more resolved information is needed, X-ray spectra can be acquired at multiple points of a line (line scan) or at all positions of a two-dimensional spot pattern.

Afterwards, the chemical composition can be evaluated at each position of the respective pattern, resulting in a compositional profile or chemical map of the specimen. In STEM, the HAADF signal can be recorded simultaneously with the X-ray spectra to correlate features in the image with the composition. A problem especially with EDX mapping is the acquisition time for the X-ray spectra that need to be recorded. Specimen beam damage, specimen drift and / or contamination build-up can limit the possibilities to obtain useful EDX maps. For many materials, the damage induced by the electron beam is the largest problem and can often only be reduced by using very efficient detection systems to allow shorter acquisition times.

### 3.9 Focused ion beam / scanning electron microscopy (FIB/SEM)

A focused ion beam / scanning electron microscope (FIB/SEM) is a combined instrument that contains an electron column with optics like an SEM and additionally an ion column to form a focused ion (usually gallium) beam. The same imaging and spectroscopy modes as described in Section 3.5 can be performed using the electron beam, while the ion beam can be used to image the specimen (by secondary electrons which are created upon ion impact) and to sputter away material in a controlled and localised way. The sputter rate of the ion beam can be controlled by the ion energy and current. In most instrument, the electron and ion beams are tilted  $52^\circ$  with respect to each other and the specimen is placed in the coincidence point of the two beams as illustrated in Figure 3.5. The specimen tilt can be controlled. The specimen is usually facing the ion beam during ion milling. The electron beam can be used to image the progress of the milling from the side. Additionally, platinum (mixed with carbon) can be locally grown on the specimen by introducing a platinum containing gas into the chamber. The electron or ion beam interacts with the gas resulting in the local deposition of a Pt containing pattern. This is routinely used to weld a micromanipulator to the specimen or to attach slices extracted from the sample to a TEM grid.

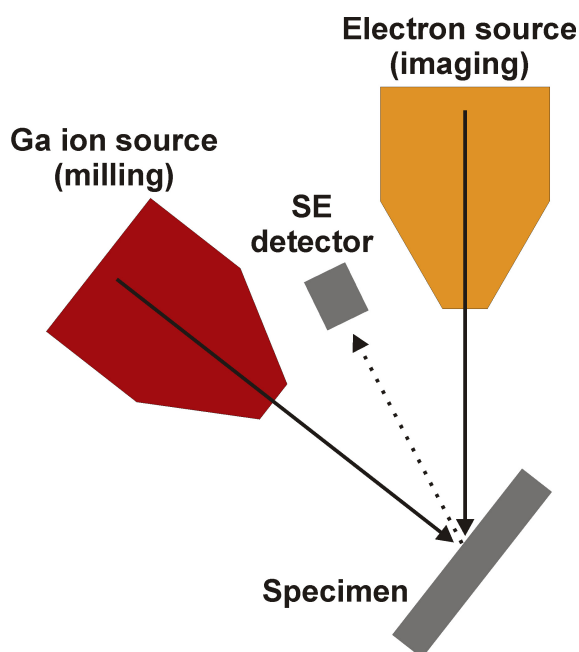


**Figure 3.5:** Schematic drawing of the principal setup of a FIB/SEM during ion milling. The specimen surface is usually facing the ion beam. An SE detector is being used to detect SEs created by the electron beam or the ion beam.

The FIB/SEM was used for two different purposes in this thesis which will be explained in the following text.

#### 3.9.1 FIB/SEM TEM specimen preparation

The FIB/SEM was used to prepare thin foil specimens for TEM investigations. Two trenches were milled into the surface of a specimen using the ion beam, leaving a lamella in between those trenches. A micromanipulator was inserted, brought in contact with the lamella and attached by platinum deposition. The lamella was afterwards cut free from the surface, lifted out and attached to a TEM copper grid. Subsequently, the lamella was thinned down further until it had a suitable thickness for TEM investigation using the ion beam. More information about the general technique can be found in references [56, 57], the procedures used for the catalyst samples in this thesis will be explained in more detail in Chapter 4.

An FEI Versa 3D DualBeam<sup>TM</sup> FIB/SEM was used for the TEM specimen preparation. For imaging of the specimens, an electron beam acceleration voltage of 2 kV was used, while 30 kV was used for the ions for milling. The ion currents ranged from 4.5 nA for milling of the initial trenches down to about 40 pA for the final thinning of the lamellae.

#### 3.9.2 FIB/SEM slice & view

The FIB/SEM was also used for three-dimensional imaging of catalyst specimens by applying the so-called *slice & view* technique. The surface of the specimen was imaged using the electron beam and, in this case, a BE detector. Subsequently, a thin layer of the surface was removed by ion beam sputtering and the same area was imaged again. This procedure was repeated until a certain volume of the specimen was removed and a stack of images representing that volume was recorded. Using a reconstruction software, a three-dimensional model of that volume was created from the images. For the slice & view experiments, an FEI Helios NanoLab<sup>TM</sup> FIB/SEM was used.



## 4 TEM specimen preparation

The method by which the supported nanoparticle catalyst samples were prepared for TEM proved to be crucial for how much information could be extracted from the TEM studies of the catalysts. As explained in Section 2.2, the investigated catalysts contain small Pt-Pd nanoparticles which are supported on and within porous alumina support particles. These support particles often have approximately spherical shapes and diameters ranging from several hundred nanometres to several micrometres. TEM specimen preparation is necessary since TEM analysis requires specimens as thin as possible and not exceeding a few hundred nanometres.

Different specimen preparation methods were successfully applied and will be presented in this chapter together with a few less successful attempts. The approaches have different advantages and disadvantages which will be highlighted by experimental data acquired during STEM experiments. Depending on which information is desired from an experiment (nanoparticle size distributions, high-resolution imaging of individual nanoparticles, spatial distribution of nanoparticles within the oxide support particles, ...), an appropriate preparation method needs to be chosen. The content of this chapter is largely related to Paper I.

### 4.1 Traditional crushing method

A common specimen preparation for supported nanoparticle catalysts is to simply crush the catalyst powder in a mortar, dissolve it in alcohol and deposit some drops of the solution onto a support grid, e.g. a carbon film on a copper grid [58–61]. After drying, many small fragments of the oxide support particles will stick to the carbon film by van der Waals forces and electrostatic interactions and the grid can directly be inserted into a TEM specimen holder. Figure 4.1 shows a STEM image of a typical alumina support fragment (bright feature) from the Pt-Pd/Al<sub>2</sub>O<sub>3</sub> catalyst supported on a holey carbon film. On two sides the fragment is hanging over holes in the carbon film, these regions are the most suitable parts for high-resolution imaging since the electron beam does not have to pass through the carbon film, which also scatters the electrons.

The size of this fragment is still relatively large so that only small regions around the outer edge are thin enough for high-quality STEM imaging at high magnifications. In the upper left corner, two additional very small alumina fragments can be seen.

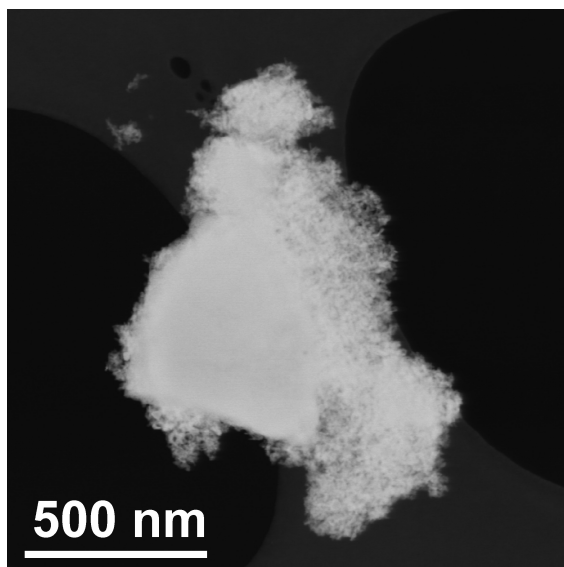


**Figure 4.1:** STEM image of an alumina support fragment produced by the traditional crushing method for TEM specimen preparation. The alumina is the brightest feature, the supporting carbon film can be seen as darker areas and the darkest regions are holes in the carbon film.

STEM images obtained at higher magnification are shown in Figure 4.2. Pt-Pd nanoparticles can be seen in these images as bright and sharp features, whereas the alumina in the background appears more fuzzy. Figures 4.2a-c show STEM images obtained from different regions. It can be seen that these three regions have different characteristics with respect to the type of Pt-Pd nanoparticles they contain: Region 'a' contains no or only very small nanoparticles, region 'b' contains small and medium sized nanoparticles below 5 nm in diameter and region 'c' contains large nanoparticles with up to 40 nm in diameter in addition. Figures 4.2d-f show different regions at different magnifications, demonstrating that Pt-Pd structures ranging from single atoms and small clusters to the large nanoparticles are represented in the specimen.

Based on these STEM results it seems difficult to define representative regions for, e.g., a nanoparticle size analysis. The spatial distribution of the nanoparticles seems random and the choice of region might strongly influence the results obtained from the TEM analysis. As we will see later, the reason for this seemingly random distribution lies in an inhomogeneous distribution of nanoparticles of different sizes across the alumina support particles. When the alumina particles are crushed and dispersed on the carbon grid, alumina fragments from different areas of the original alumina particles will be observed and it is not possible to discern the origin of the fragments. Also, as mentioned above, usually only the outer edges of the alumina fragments are thin enough for high-quality imaging, increasing the time needed to

find suitable regions.

This method has advantages, though, one of them being its simplicity. It can be performed very quickly without the need of advanced equipment. Also, the outer edges of the fragmented pieces can be very thin, usually thinner than specimens prepared by the methods described below. This preparation method may be suitable for high-resolution imaging of individual nanoparticles if statistics of larger numbers are not required.

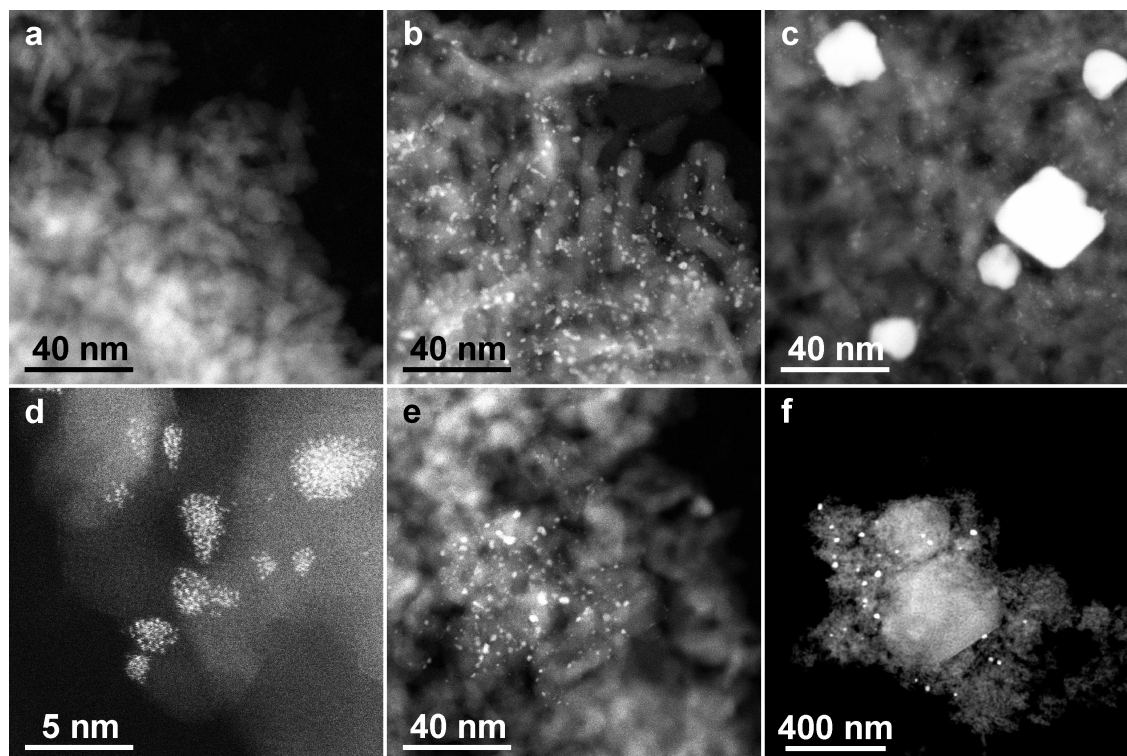


**Figure 4.2:** HAADF STEM images of a Pt-Pd/ $\text{Al}_2\text{O}_3$  catalyst prepared by the traditional crushing method. a) to c) show different regions at a constant magnification, d) to f) show different regions at different magnifications.

## 4.2 Dimple grinding and argon ion milling

In order to obtain specimens with larger thin areas, which would enable imaging of a large number of randomly chosen Pt-Pd nanoparticles, an approach combining mechanical dimple grinding and argon ion milling was tested. The catalyst powder was embedded in LR White<sup>TM</sup> acrylic resin (hard grade). A small amount of powder was put in a gelatine capsule which was then filled with the liquid resin and sealed by a gelatine cap. The resin was allowed to infiltrate the powder during 12 hours,

after which it was hardened in an oven at 60°C for 24 hours. Afterwards, the gelatine was dissolved in water. Figure 4.3a shows a photograph of the cured block where the dark part contains the catalyst powder.

Slices of the block were cut using a low-speed saw (Figure 4.3b) and thinned down to about 0.2 mm using grinding paper. A mechanical dimple grinder was used to thin down the slice to about 20  $\mu\text{m}$  in the center. Afterwards, it was inserted into a Fishione 1010 IonMill™ system, which sputters away material with a broad argon ion beam at a low incident angle. As soon as a hole in the center of the specimen is detected, the milling is stopped. The surrounding areas should be thin enough for TEM imaging. Acceleration voltages between 1 and 4 kV were used for the argon ions. Ion currents between 2 and 6 mA and incident angles from 8° to 12° were tested.

Regardless of the parameters, the specimens always turned out to be non-ideal for TEM investigations. Even regions very close to the hole in the specimen were too thick for high quality imaging. This was probably caused by differential milling, since the resin between the alumina support particles was removed much easier by the ion beam than the alumina itself. It led to a situation where the resin surrounding the alumina particles was completely sputtered away before the alumina was reasonably thin, at which point the particles fell off. Figure 4.3c shows a TEM image of the central hole and an adjacent area with thick alumina particles held together by resin. Some regions at the edge of the alumina particles were thin enough for TEM imaging, but that was no improvement compared to the crushing method or depositing the whole alumina particles onto a carbon film.

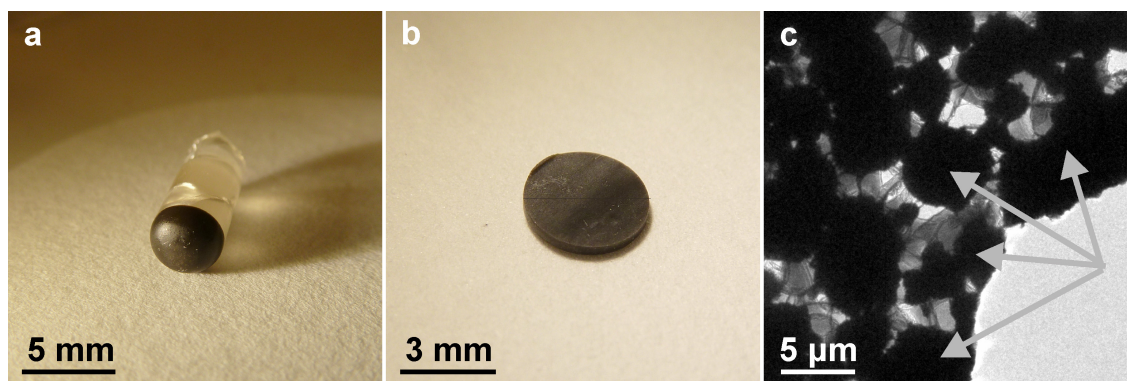


**Figure 4.3:** Specimen preparation by dimple grinding and argon ion milling. a) Catalyst powder (dark region) embedded in acrylic resin. b) Slice of resin before further thinning and dimple grinding. c) TEM image of the specimen after argon ion milling. Alumina particles (marked by arrows) near the hole are too thick for high-quality TEM imaging.



## 4.3 FIB/SEM lift-out method

To reduce the problems of differential ion milling and gain more control over the specimen geometry, specimen preparation with focused ion beam / scanning electron microscopy (FIB/SEM, introduced in Section 3.9) was performed. The preparation steps will be explained with the help of Figure 4.4. As mentioned earlier, most of the alumina particles can be described as nearly spherical. An SEM image of such an alumina support particle is shown in Figure 4.4a. The catalyst powder was embedded in acrylic resin identically to the procedure explained at the beginning of Section 4.2. The slice was then glued onto an SEM sample holder with conductive silver paint and polished using fine grinding paper. To increase the electrical conductivity for SEM imaging and FIB milling, a thin layer of carbon was coated onto the specimen surface.

Figure 4.4b shows a top-view SEM image of the embedded and polished specimen. Alumina particles can be seen as brighter features in the image. In the center there is a nearly spherical particle, the white box marks the region that is chosen to be extracted from the center of that particle. The procedure to extract a TEM specimen is as follows. Gallium ion milling is performed in the regions marked by the dotted red lines to cut trenches on either side of the region of interest. These trenches are usually several micrometres deep. Figure 4.4c shows a lamella after milling, containing the desired region. A micromanipulator (upper right corner of Figure 4.4d) is brought in contact with the lamella. Local platinum deposition is used to weld the manipulator to the lamella. Subsequently, the lamella is cut free from the bulk specimen using the ion beam. The stage is lowered and the lamella is lifted out of the surface. Figure 4.4e shows the lamella after extraction. Alumina particles are brighter compared to the resin. The upper particle (or portion of a particle) corresponds to the one observed in the top view SEM image before extraction.

It should be noted that the slice shows the particle in a cross-section view, which is one of the main advantages of this preparation method. The lower edge of the particle that can be seen in Figure 4.4e corresponds to the outer edge of the original alumina particle, whereas the regions further up originate from the interior of the particle.

The specimen is then mounted onto a copper grid compatible with the TEM specimen holders. A V-shaped post of the TEM grid is used, as seen in Figure 4.4f. This allows fixing the specimen at both ends to the copper grid to mechanically stabilise the specimen as it is further thinned down. Initial tries were performed with the specimen attached at just one side to a copper post. As the thickness was reduced by ion milling, it started to bend quickly which prevented any further thinning and rendered a useless specimen. A deep trench is milled into the V-shaped copper post before the specimen is attached, as can be seen in Figure 4.4f. This

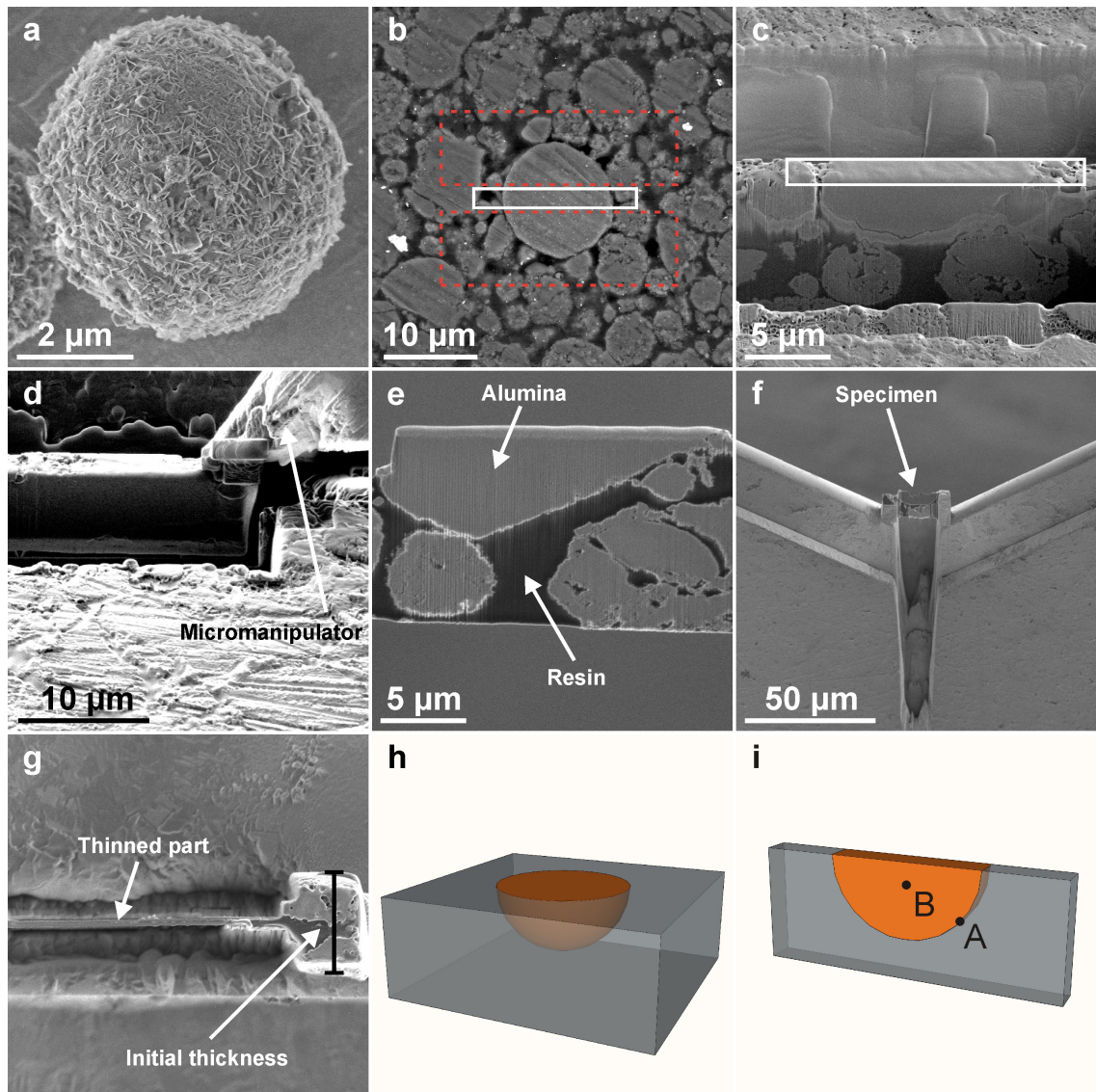


**Figure 4.4:** Specimen preparation by FIB/SEM lift-out. a) to g) show step-by-step SEM images of the lift-out procedure, whereas h) and i) show schematic illustrations explaining the specimen geometry. Point A lies on the outer edge of the support particle, whereas point B lies in the interior region.

minimises the amount of copper that is sputtered away and which would partly redeposit onto the specimen.

The specimen is then further thinned using the ion beam facing the edge of the slice. Figure 4.4g shows an SEM image of the specimen after final thinning. On the right side a remaining thick part can be seen, whereas the lamella on the left side is electron transparent and sufficiently thin for high-resolution TEM investigation.

Figure 4.4h shows a schematic illustration of a spherical alumina particle embedded in resin and polished before lift-out, while Figure 4.4i shows the specimen geometry after the lift-out procedure (corresponding to Figure 4.4e). Two points are marked in the schematic: Point A lies near the outer edge of the original alumina particle, point B lies in the interior. Due to this specimen geometry, the properties of these regions can now be investigated and compared, in contrast to specimens from the traditional crushing method, where the origins of the fragmented alumina pieces are unknown.

Figure 4.5a shows a STEM image of the fresh Pt-Pd/ $\text{Al}_2\text{O}_3$  specimen prepared by the lift-out method. The cross-section of an individual alumina support particle can be seen, including the outer edge of that particle in the lower part of the image. A region situated at the outer edge is marked by a white square and shown at higher magnification in Figure 4.5b. Pt-Pd nanoparticles can be seen in this STEM image as sharp bright spots. The porous and corrugated alumina support in the background also causes strong intensity variations in the image but still the Pt-Pd particles are visible. Additionally, two large nanoparticles can be seen very close to the outer edge.

To simplify the discussion, the Pt-Pd nanoparticles will be divided into three categories:

- **Small nanoparticles:** diameters of 1.5 nm or below.
- **Medium-sized nanoparticles:** diameters from 1.5 nm to 10 nm.
- **Large nanoparticles:** more than 10 nm in diameter.

Two interesting observations were made due to the unique specimen geometry of the lift-out specimens. Firstly, the large nanoparticles were only found very close to the outer edge of the alumina support particles. In the interior regions of the alumina, no large nanoparticles were observed. Secondly, the medium-sized nanoparticles (that can be seen in Figure 4.5b as sharp bright spots) were concentrated in a layer with a thickness of around 100 nm from the outer edge. In the region shown in the upper part of Figure 4.5b, there are only small nanoparticles which can hardly be seen at this magnification. Figure 4.5c shows a STEM image of an interior region at higher magnification with a large number of small nanoparticles dispersed on the alumina. Figure 4.5d shows a similar high-magnification STEM image of the region close to the outer edge, where small and medium-sized nanoparticles were found.

Quantitative analysis could be performed much easier than for specimens from the crushing preparation because the two regions (interior and outer layer) in itself were much more homogeneous than the fragmented pieces from the crushing method. This is valid for both the nanoparticle distribution but also for the specimen thickness which shows less variations. A large number of images like in Figure 4.5c and d could be acquired and particle size distributions (as described in

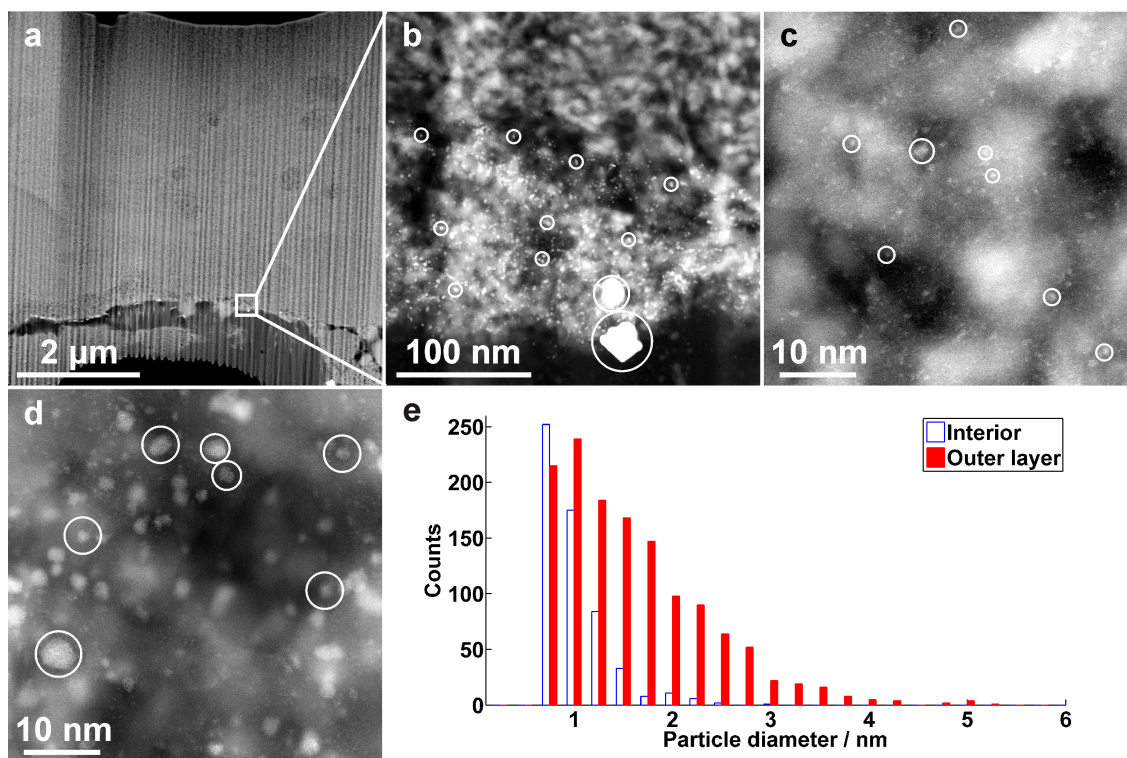


**Figure 4.5:** Results obtained from a Pt-Pd/Al<sub>2</sub>O<sub>3</sub> catalyst prepared for TEM by the FIB/SEM lift-out method. a) Overview HAADF-STEM image of the slice of an individual alumina support particle. b) Image of the marked region near the outer edge at higher magnification. A layer with a high density of medium-sized nanoparticles as well as large nanoparticles close to the outer edge can be seen. Some nanoparticles are marked by circles. c) High-resolution image of a region inside of the alumina particle. d) High-resolution image of a region close to the outer edge of the alumina particle. e) PSDs for both regions obtained by evaluation of STEM images.

Section 3.7) could be obtained separately for the two regions. These are shown in Figure 4.5e. The large nanoparticles are not included here due to their very low number, as well as nanoparticles below 0.6 nm since they could not always be reliably observed. As could already be seen from the STEM images, in the interior there are almost exclusively small nanoparticles below about 1.5 nm, whereas the outer layer contains small as well as medium-sized nanoparticles up to about 4 nm.

These experiments demonstrate clearly the advantages of the FIB/SEM lift-out specimen preparation method: Large homogeneously thin specimen regions and preservation of the structure of the alumina support particles which enables the observation of variations in nanoparticle distribution along the radial direction, as shown in this case. There is still some room for improvement, though. As can be seen in Figure 4.5a, the thickness of the specimen varies in a more or less periodic

fashion from left to right, this is a so-called curtaining effect. It arises due to inhomogeneities (like the porous structure of the alumina) in the specimen that lead to different milling rates along different regions. So far, this effect could not be avoided, although a combination of very low ion currents and low ion energies (5 keV and 2 keV) during final thinning were tested.

An approach of final thinning in an argon ion mill (see Section 4.2) after the FIB/SEM preparation was investigated as well. However, due to the use of the V-shaped copper posts as explained earlier, large amounts of copper were sputtered away behind the specimen and redeposited onto the specimen which thereafter was covered by a layer of copper. A simple post with the specimen mounted on only one side would need to be used, but then the mechanical specimen stability showed to be insufficient. It should also be noted that previous experience of preferential milling effects is that once established, it can not be removed by subsequent gentle Ar ion milling.

Another downside for high-resolution investigations compared to the crushing method can be the specimen thickness. Although it is much more homogeneous and suited for quantitative analysis for the of lift-out specimens, the thinnest parts of the fragmented pieces from the crushing methods can be considerably thinner compared to the lift-out lamellas. So if high-resolution imaging of individual nanoparticles is of primary concern, the crushing method could be favourable in some cases. Again, there probably still is room for improvement of the technique in this respect.



## 5 Ageing studies

In this chapter, ageing studies of the Pt-Pd/Al<sub>2</sub>O<sub>3</sub> catalyst will be summarised, focusing on the effect of nanoparticle sintering induced by the ageing procedure. The samples were aged in a gas flow reactor and characterised using SEM, STEM and FIB/SEM, including X-ray spectroscopy, as well as N<sub>2</sub> physisorption and CO oxidation experiments. The content of this chapter is based on work performed for Paper II.

### 5.1 High-resolution STEM imaging of crushed specimens

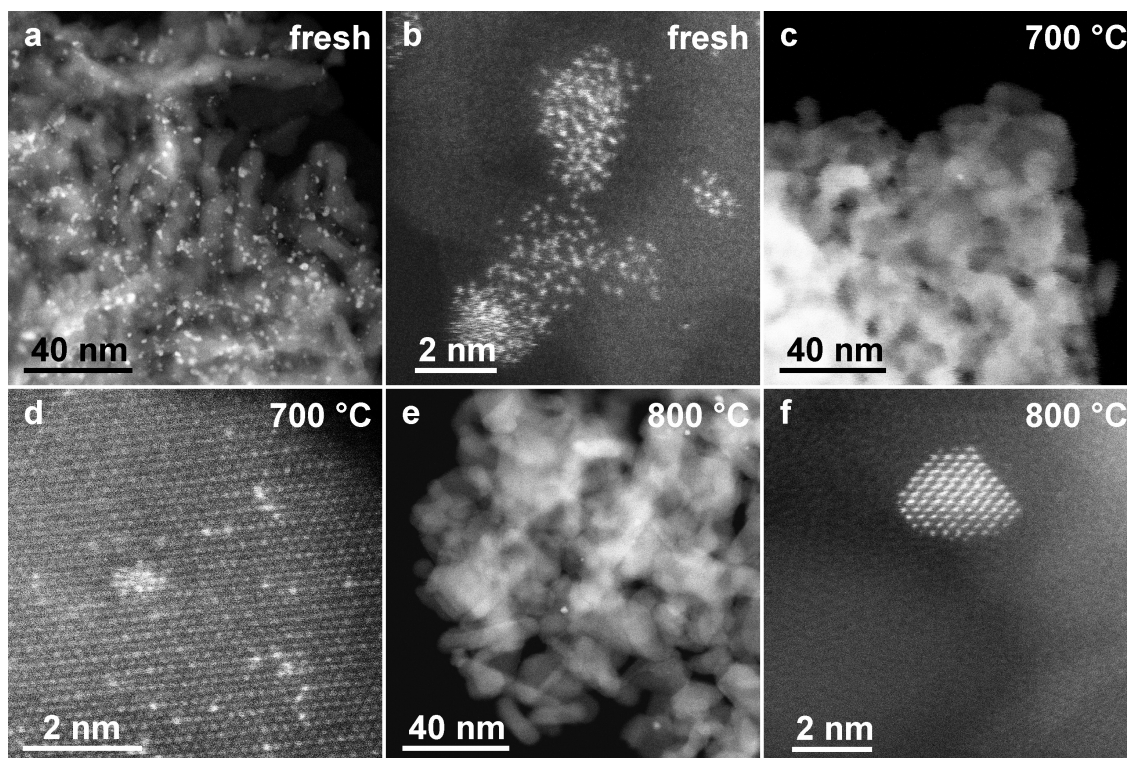
Although the main part of the STEM analysis in this chapter will be based on specimens prepared by the FIB/SEM lift-out method, images obtained with the traditional crushing method (see Chapter 4) can give a first impression of the specimens. Also, as mentioned earlier, high-resolution imaging is often performed more easily with these specimens. For this reason, this section focuses on presenting high-resolution images of the fresh specimen as well as specimens aged at 700 °C and 800 °C, while the following sections will focus on quantitative characterisation using FIB/SEM lift-out specimens. The details of the ageing protocol can be found in Section 3.2.

Figure 5.1 shows HAADF-STEM images acquired at high magnification, the brightest structures represent the Pt-Pd nanoparticles (or clusters and single atoms). It can be seen that the fresh specimen contains a high density of very small Pd-Pd structures (but also large nanoparticles as was shown in Figure 4.2c and f). Figure 5.1b shows small clusters, single atoms and particle-like structures which appear unordered and non-crystalline. This observation appeared to be consistent over different areas of the specimen.

The high contrast that can be seen in the clusters despite their non-crystallinity suggests that these are flat, raft-like clusters. This is also in accordance with work by Boyes et al. [62,63] who imaged platinum particles on a carbon film and obtained a very similar appearance of the particles. They performed an atomic column height analysis and concluded that the clusters had a 'thickness' of four atoms or less. This is probably similar in case of the structures seen in Figure 5.1b.

Figure 5.1c and d show the specimen aged at 700 °C. In most regions, the number





**Figure 5.1:** HAADF-STEM images of the fresh and aged specimens (700 °C and 800 °C) prepared by the traditional crushing method.

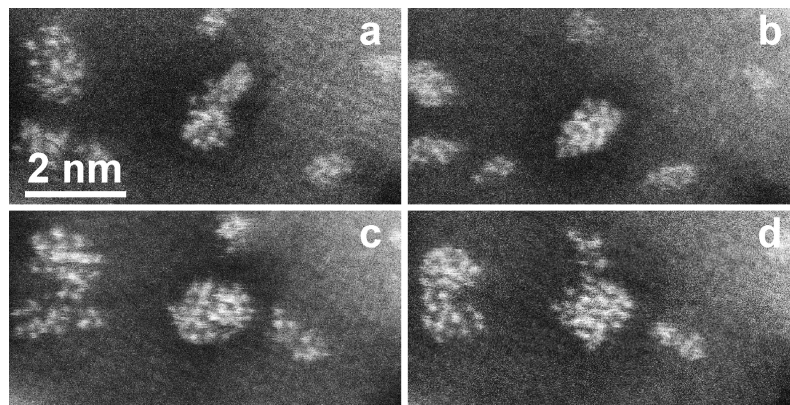
of small nanoparticles is strongly reduced, Figure 5.1d demonstrates, though, that small clusters and single Pt or Pd atoms are still present in the specimen (the atomically resolved lattice in the background is the supporting alumina).

Figure 5.1e shows that the density of small nanoparticles after ageing at 800 °C appears similarly low as after ageing at 700 °C. A small nanoparticle can be seen in Figure 5.1f. This particle appears to be crystalline and faceted, in contrast to the ones seen in Figure 5.1b. It appears that the few remaining small nanoparticles in the specimen aged at 800 °C obtained low-energy equilibrium structures during the ageing procedure, in contrast to the energetically unfavourable high disorder of the particles in the fresh sample.

When acquiring images at a magnification as high as in Figure 5.1b, d and f, clear effects of beam damage were noticeable. This is due to the focused electron beam being scanned over a very small area of about 80 nm<sup>2</sup>, exposing the specimen area to large electron dose rates. Two effects were observed: Firstly, the Pt and Pd atoms could become mobile under the electron beam (migration of atoms, rearrangement of clusters) and crystalline nanoparticles could undergo partial amorphisation. Secondly, the alumina support could be damaged by the electron beam, holes could be created in the specimen.



In both cases, the beam effects could be due to knock-on damage, heating by the electron beam or a combination of both (see Section 3.6.3). Figure 5.2 shows as an example a STEM image series of a region with a few small nanoparticles/clusters that are undergoing changes due to several consecutive electron beam scans. At an acceleration voltage of 300 kV, knock-on damage is certainly occurring. In case of the alumina support, this probably leads to sputtering of the material, since the sputtering threshold energy of aluminium is around 4-8 eV, while the maximum transferable kinetic energy of a 300 keV electron is approximately 30 eV [51].



**Figure 5.2:** HAADF-STEM image series (same area) demonstrating electron beam damage to small nanoparticles. The nanoparticles are changing their shapes and partly coalescing while the electron beam is scanned over them several times.

Sputtering of the alumina support would in most cases also influence the structure of small clusters or nanoparticles supported by it. STEM imaging at 80 kV acceleration voltage was tested in an attempt to reduce the beam effects, but the small clusters were still affected by the electron beam, even though the effect was reduced. While the knock-on damage and sputtering should be reduced at 80 kV, the heating effect is probably larger due to the larger cross section for inelastic scattering at lower energies. Considering the relatively small improvements in nanoparticle stability combined with the decreased image quality at 80 kV, all further STEM imaging was performed at 300 kV.

It should be noted that, as explained in Section 4.1, the specimens prepared for TEM by the crushing method appear very inhomogeneous and the definition of a 'representative region' is difficult.

## 5.2 Nanoparticle sizes and distribution - STEM investigation

An analysis of the spatial distribution and PSD of the Pt-Pd nanoparticles was performed for fresh samples and for samples aged at 500 °C, 600 °C, 700 °C and 800 °C. The TEM specimens for these analyses were all prepared by the FIB/SEM lift-out method. Figure 5.3 shows STEM images of all specimens. The magnifications were lower and the specimens slightly thicker compared to the previous section, thus avoiding the effects of beam damage. Figure 5.3a and b show an overview image of the fresh specimen and a higher magnification image of a region close to the outer edge and one in the interior of the alumina support particle. The Pt-Pd nanoparticles (seen in the images as sharp, bright features) are divided into three groups:

- **Small nanoparticles:** diameters of 1.5 nm or below.
- **Medium-sized nanoparticles:** diameters from 1.5 nm to 10 nm.
- **Large nanoparticles:** above 10 nm in diameter.

As shown earlier, the fresh sample contains almost exclusively small nanoparticles in the interior of the alumina support, whereas small, medium-sized and large nanoparticles are found in an outer layer of about 100 nm thickness close to the outer edge. The small nanoparticles cannot be seen at the magnification used here, but they were shown earlier in Figure 4.5c.

Figure 5.3c and d show the catalyst after ageing at 500 °C. There are no obvious changes in the structure. The outer layer with the medium-sized and large nanoparticles can still be observed and the interior contains only small nanoparticles. This proposes that, if any, only very slight sintering effects have occurred.

Ageing at 600 °C resulted in a significant change in the structure, as can be seen in Figure 5.3e and f. The large nanoparticles are still limited to the outer layer, but the medium-sized nanoparticles can not be observed at the outer edge any more. The most plausible explanation is sintering of these nanoparticles to form additional large nanoparticles or enlarge the ones already present. Since the nanoparticles in the interior are still very small, the overall distribution of the nanoparticles is strongly bimodal, almost all particles are either below 1.5 nm or above 10 nm. This suggests that the small nanoparticles have a higher stability against sintering compared to the medium-sized ones. The sintering could be promoted by the high density of particles in the outer layer that makes coalescence of nanoparticles more likely. Also, the porous structure of the alumina might be more open near the outer edge and not as effective in separating the nanoparticles. On the other hand, small nanoparticles are still visible in the outer layer.

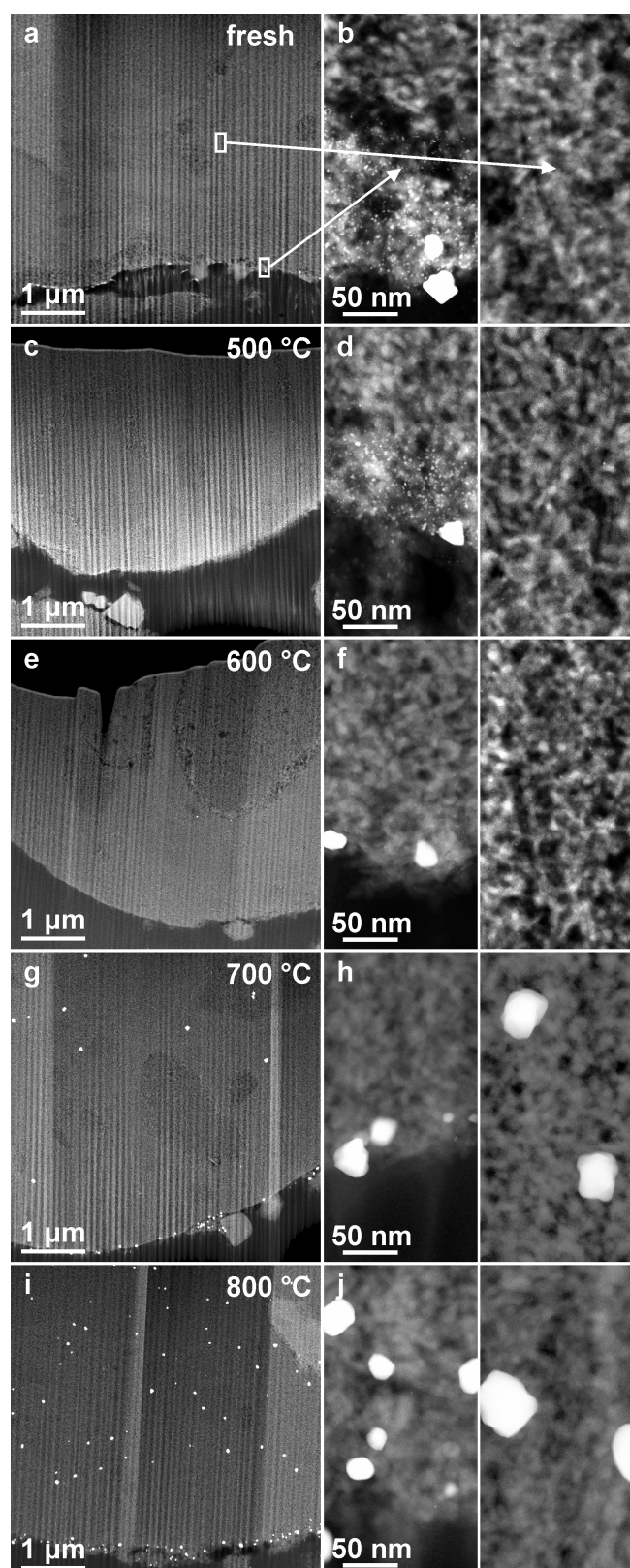


**Figure 5.3:** HAADF-STEM images of the fresh and aged specimen prepared by the FIB/SEM lift-out method. In the left row, low-magnification overview images are shown, the right row shows images of the outer layer and interior region of each specimen at higher magnification.

In Figure 5.3g and h the sample can be seen after ageing at 700 °C. Ageing at this temperature induces sintering of the small nanoparticles as can be seen from the large nanoparticles that can now also be found in the interior region of the alumina particles. Since these regions earlier only contained small nanoparticles, the now observed large nanoparticles must result from sintering. The density of large nanoparticles at the outer edge seems also higher than before. Small nanoparticles can still be found in the specimen, but their number density is strongly reduced. Ageing at 800 °C (Figure 5.3i and j) promotes further sintering of the small nanoparticles, almost none can be found in the specimen. The density of large nanoparticles in the specimen increases at the same time.

The sizes of the nanoparticles were analysed using the procedure explained in Section 3.7 for the fresh samples as well as the ones aged at 500 °C and 600 °C, resulting in the PSDs shown in Figure 5.4. The small and medium-sized nanoparticles were included in this analysis, the large ones were too sparse for a statistical analysis in the TEM specimens. They were instead analysed in an SEM study that will be presented in Section 5.3. The samples aged at 700 °C and 800 °C were not included in this part for the same reason: Since the small and medium-sized nanoparticles sintered, the overall number of particles was very low in the TEM specimens.

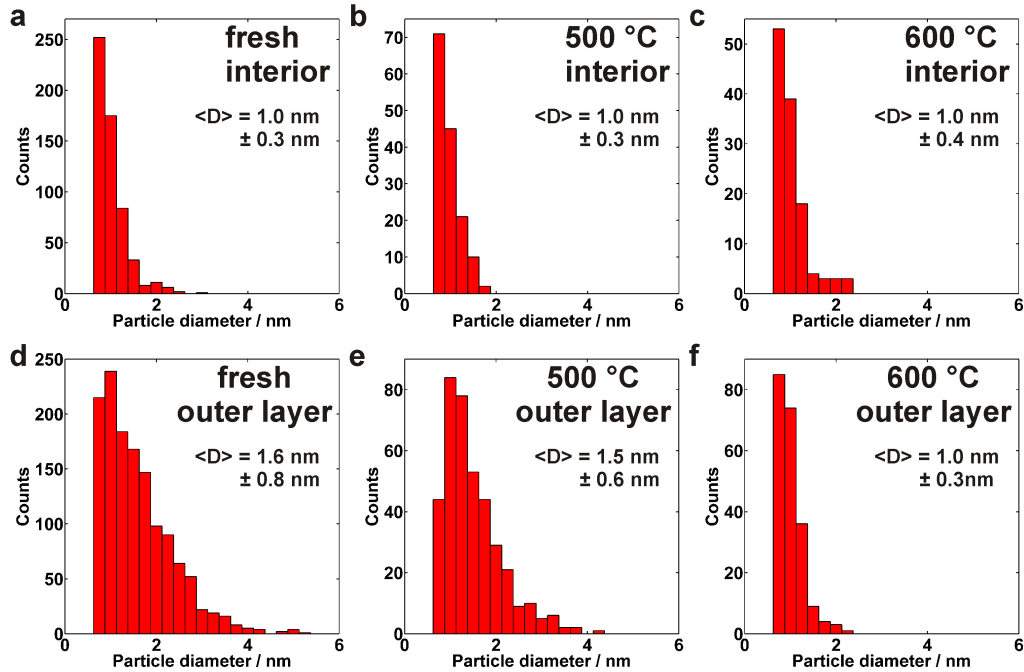


**Figure 5.4:** PSDs obtained from STEM images of the fresh as well as 500 °C and 600 °C aged specimen.

As can be seen in Figure 5.4, the difference between the fresh and the 500 °C aged specimen is very small. Both contain only small nanoparticles in the interior and small as well as medium-sized nanoparticles in the outer layer near the edge. There might be a slight reduction of medium-sized nanoparticles in the outer layer after ageing. The PSDs of the 600 °C aged specimen show clearly the disappearance of the medium-sized nanoparticles, as could be seen also in Figure 5.3f. Figure 5.4f might be misunderstood as a shrinkage of the nanoparticles, though that is not what happened. The medium-sized nanoparticles sintered to form large particles (that are not shown here), while the small nanoparticles remained.

## 5.3 Nanoparticle sizes and distribution - SEM investigation

A complimentary particle size analysis was performed using SEM. The large nanoparticles, which due to their low number could not be included in the TEM analysis, will be considered in this section. Particles down to about 10 nm could be reliably detected using SEM. The investigated specimens were embedded in acrylic resin, polished at the top surface and coated with a thin carbon film for better electrical conductivity. When the specimen is being polished, the interior of many alumina particles is exposed which enables a similar cross-section view as for the lift-out TEM specimens. SEM images together with corresponding PSDs are shown in Figure 5.5. The darkest regions represent the resin, the brighter regions the alumina and the sharp bright spots are the Pt-Pd nanoparticles. The fresh, 500 °C aged and 600 °C aged specimens contain the large nanoparticles mainly at the outer edge, as observed by STEM analysis, while specimens aged at 700 °C and 800 °C contain large nanoparticles in all regions.

The right column in Figure 5.5 shows the PSDs obtained from the SEM images. There is a slight but steady increase in average nanoparticle size with increasing ageing temperature up to 600 °C. At 700 °C the average size is similar to 600 °C (but the spatial distribution is strongly changed). The most drastic change can be seen between 700 °C and 800 °C, where the average nanoparticle diameter (only considering the large nanoparticles) increases from 26.7 nm to 35.8 nm. It should be noted that the maximum of the PSD after ageing at 800 °C still is around 28 nm, the strong increase in average size results from an increase of particles in the tail of the distribution above 35 nm.

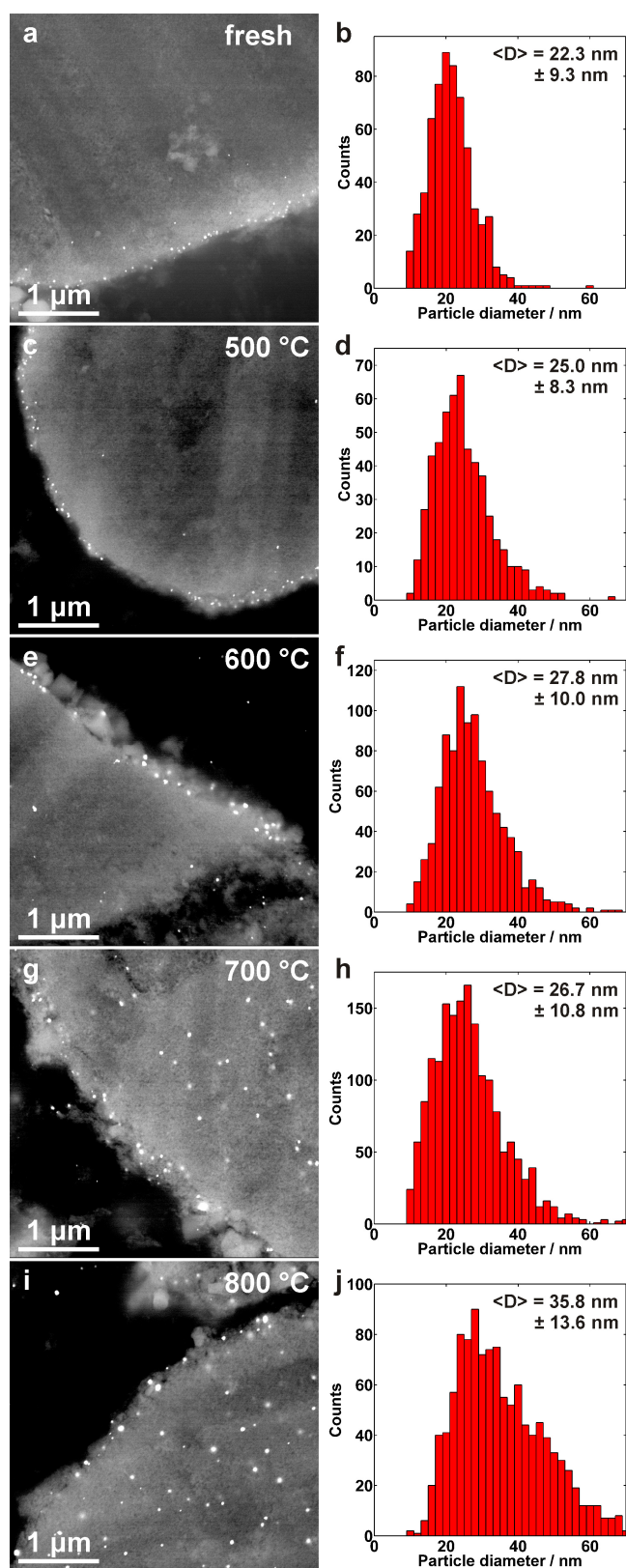


**Figure 5.5:** SEM images and corresponding PSDs of the fresh and aged specimens embedded in resin.

## 5.4 Three-dimensional nanoparticle distribution - FIB/SEM slice & view

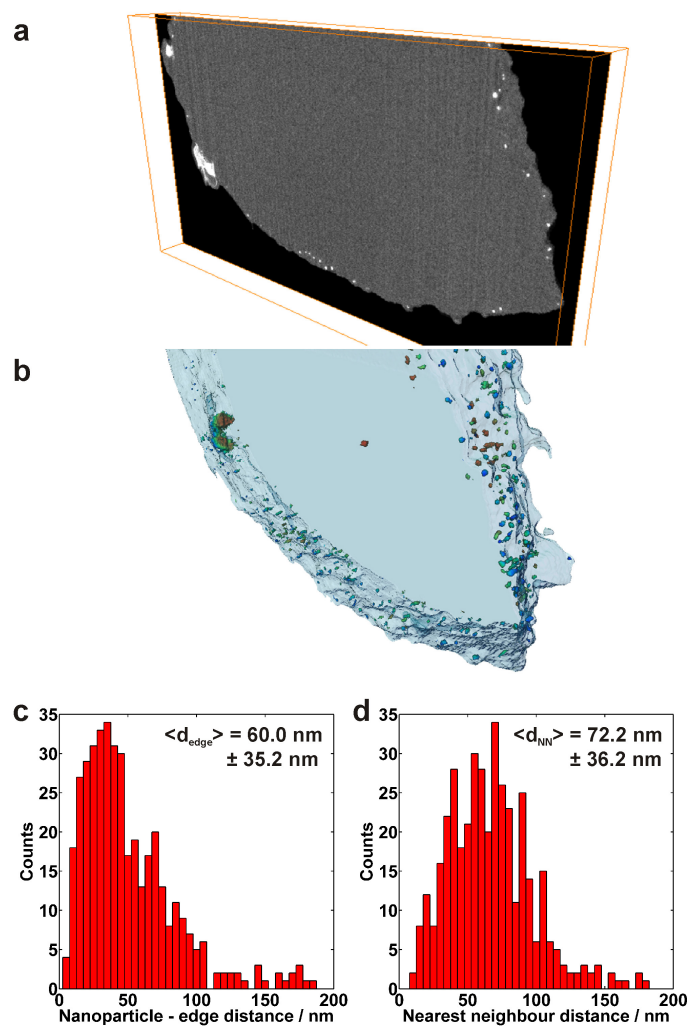
Three-dimensional FIB/SEM slice & view experiments (see Section 3.9.2) were performed to confirm the spatial distribution of nanoparticles as seen by the cross-sectional SEM and TEM measurements, as well as to obtain quantitative data of inter-particle distances and the distances from the nanoparticles to the outer edge of the alumina support. Like in the SEM analysis, only nanoparticles larger than 10 nm could be observed using this technique.

Figure 5.6a shows one image selected from a stack of images that were acquired while cutting through an alumina particle. The Pt-Pd nanoparticles can be seen as bright features. Already from the image, the presence of the large nanoparticles only at the outer edge of the alumina particle is obvious. A 3D image of the specimen can be reconstructed from all the acquired images. One reconstruction is shown in Figure 5.6b. The light blue structure represents the alumina particle, while the Pt-Pd nanoparticles can mainly be seen close to the outer edge.

The distances of the nanoparticles to the edge of the alumina particle were determined by first thresholding the alumina particle and the nanoparticles separately to obtain their three-dimensional coordinates and dimensions, followed by calculating the distance from the center of gravity of each nanoparticle to the outer edge of the alumina structure. The distribution of the nanoparticle-edge distances is shown in Figure 5.6c. Most particles are within 100 nm to the outer edge as was estimated from the STEM images. An alternative quantification is the distance from each particle to its nearest neighbour, which can easily be calculated given the particle coordinates.

A distribution of the nearest-neighbour distances is shown in Figure 5.6d. For the fresh specimen, most distances are below 150 nm and of the same order of magnitude as the particle-edge distances. To compare spatial distributions for different specimens quantitatively, the nearest-neighbour distance might be a better measure since it should not strongly depend on the size of the alumina particle. The particle-edge distances, on the other hand, will strongly scale with the alumina particle size if the nanoparticles are not confined to a thin outer layer but distributed over the whole support, as is the case for the specimen aged at 800 °C. Slice & view measurements of aged specimens are being performed and will provide interesting information and illustration of the three-dimensional nanoparticle distribution after ageing.

Potentially, nanoparticle size distributions could be obtained easily from the slice & view measurements, since the volume of each particle can be extracted from the dataset. An advantage compared to the SEM measurements performed in Section 5.3 would be the large number of nanoparticles in each dataset and resulting good statistics, which is very time consuming to obtain when performed manually by



**Figure 5.6:** Results from a FIB/SEM slice & view measurement of the fresh specimen. a) Single SEM image from the acquired image stack. b) Three-dimensional reconstruction showing the vast majority of nanoparticles close to the outer edge of the alumina support particle. c) Distribution of particle-edge distances. d) Distribution of nearest-neighbour distances between the nanoparticles.



analysing individual images. Additionally, the real three-dimensional shape could potentially be extracted instead of the two-dimensional projection, although the accuracy for small nanoparticles might not be very good. In the measurement shown here though, most of the nanoparticles appeared to be elongated in the direction of the milling, probably due to differential milling of the alumina compared to the nanoparticles. For this reason it was not possible to obtain any accurate measure of particle sizes.

## 5.5 Chemical characterisation by EDX

EDX measurements were performed to investigate the chemical composition of the Pt-Pd nanoparticles in different specimens (fresh and aged at 600 °C, 700 °C and 800 °C). STEM as well as SEM were used and showed consistent results. Only large nanoparticles could be considered in this study due to beam damage and low signal from small nanoparticles. In the TEM, nanoparticles down to sizes of about 10 nm could be analysed, while the smallest size in the SEM was 20 nm.

In the TEM experiments, mostly specimens prepared by the FIB/SEM lift-out method were used, except for the fresh sample where the specimens were prepared by the crushing method. The SEM experiments were performed using thin TEM specimens prepared by the crushing method. In both instruments EDX point analysis of individual nanoparticles was performed, while in the TEM additionally EDX maps of a few nanoparticles were acquired to investigate if core-shell structures could be observed.

The results obtained from the fresh sample consistently showed an enrichment of Pt in the large nanoparticles compared to the nominal values of 85 wt.-% Pt and 15 wt.-% Pd, as well as a size dependence of the composition. Nanoparticles over 30 nm in diameter had Pd concentrations of 5 wt.-% or less, particles larger than 20 nm had 10 wt.-% Pd or less, while few particles around 10 nm had Pd concentrations up to 30 wt.-%. This shows that the largest particles are rich in Pt and the Pt concentration correlates to their size. It also implies that the small and medium-sized nanoparticles, which could not be analysed here directly, have to be enriched in Pd compared to the nominal value. Other studies of similar bimetallic Pt-Pd catalyst have shown similar observations [43, 48].

In Figure 5.7 an HAADF-STEM image as well as concentration maps of Pt and Pd from a region containing several large nanoparticles are shown. No core-shell structure is visible, but the smaller particle in the upper region clearly seems to be enriched in Pd compared to the other particles. Due to the low overall Pd content, the Pd map is relatively noisy.

Ageing at 600 °C did not seem to change the chemical composition of the large nanoparticles noticeably, the Pd concentration of most particles was still around 5 wt.-%.

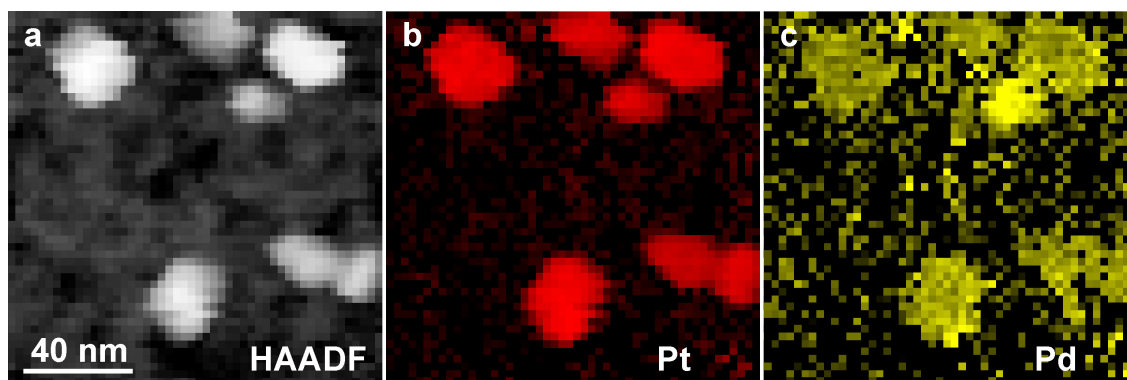


**Figure 5.7:** HAADF-STEM image and EDX concentration maps of a region of the fresh sample containing several large Pt-Pd nanoparticles. The Pt concentration appears homogeneous over the particles, no obvious core-shell structure is observed. The Pd map is noisy due to the overall low Pd concentration. A smaller particle in the upper region appears to have a relatively higher Pd concentration.

Ageing at 700 °C induced considerable changes in the composition of the large nanoparticles. The Pd concentration was found to be between 18 and 30 wt.-% for all analysed nanoparticles in the size range from 10 to 50 nm. This suggests an increased degree of alloying after ageing, even though the Pd concentrations seemed to be even a bit higher than the nominal value. Since it was observed earlier that at 700 °C a large portion of the small nanoparticle undergoes sintering while at the same time the Pd concentration in the large nanoparticles increases, this observation is consistent with a Pd enrichment in the original smaller particles.

The sample aged at 800 °C showed typical Pd concentrations of 15 to 20 wt.-% in the observed nanoparticles between 10 and 70 nm, which is closer to the nominal value of 15 wt.-%. Comparing with the fresh sample, the degree of alloying was strongly increased by the ageing procedure, which is in accordance with a study by Ezekoye et al. [43]. Some anomalously large particles with diameters above 100 nm were analysed and showed a lower Pd concentration of around 10 wt.-%, slightly enriched in Pt. This agrees with the observation that the larger nanoparticles appear to be richer in Pt, and also with studies that showed that Pt tends to form anomalously large nanoparticles during high-temperature ageing [43, 44].

Figure 5.8 shows two HAADF-STEM images and corresponding EDX maps of large nanoparticles in the sample aged at 800 °C. Again, the concentrations of Pt and Pd appear quite homogeneous over the particles, and the Pd maps are less noisy due to the higher Pd concentration.

As mentioned earlier, it is difficult to obtain a very precise quantification from the EDX analyses. In this study,  $k$ -factors (see Section 3.8) predefined by the evaluation software were used, and no absorption correction was performed due to the complex specimen geometry. Additionally, some of the spectra from smaller particles and

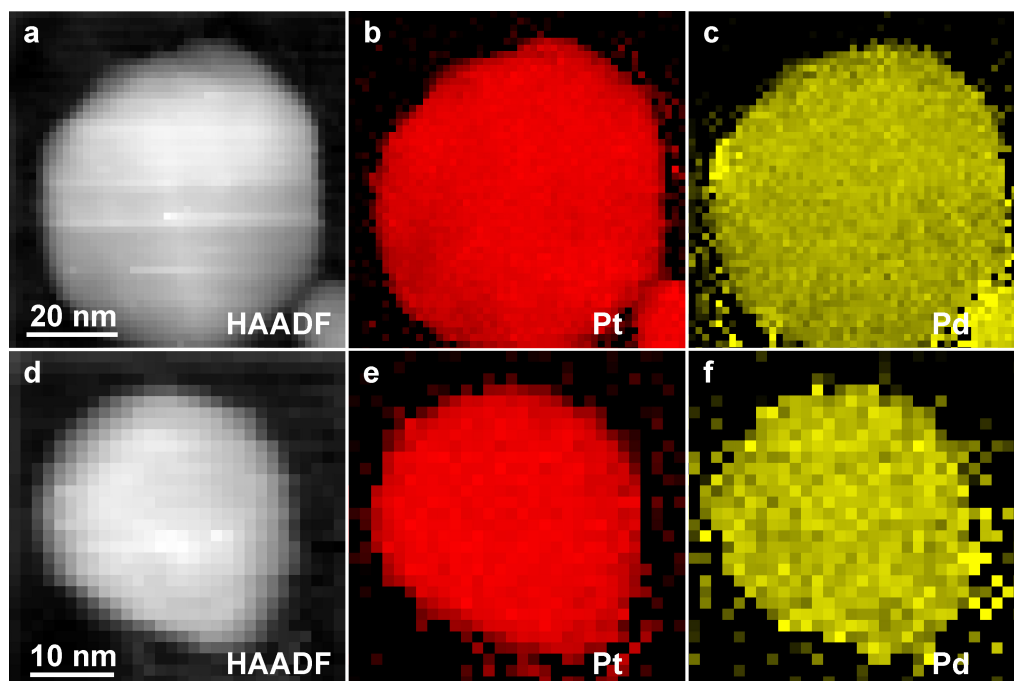


**Figure 5.8:** HAADF-STEM images and EDX concentration maps of nanoparticles in the sample aged at 800 °C. The Pt and Pd concentrations appear homogeneous over the particles, no obvious core-shell structures can be observed.

the STEM EDX mapping were a bit noisy, which further complicates a precise quantification. For this reason, there are some uncertainties regarding the precision of the obtained concentrations, which is the reason why no precise numbers are stated.

On the other hand, the approach taken here is still accurate enough to obtain the compositions within a few wt.-%, and especially to compare differences between different specimens, since the evaluation was performed using the same protocol. To illustrate this, EDX spectra of nanoparticles from the fresh and 800 °C aged specimens are shown in Figure 5.9. It can clearly be seen that in case of the aged sample the Pd-L peak in the spectrum (around 2.8 keV) has a much higher intensity, while the Pt peaks are very similar in the two spectra. The EDX data does therefore reveal valuable information about approximate Pt and Pd concentrations, differences between nanoparticles of different sizes and changes that occur during ageing.

Beam damage was the factor that mostly inhibited the acquisition of spectra with better count statistics (especially for smaller nanoparticles around or below 10 nm) and EDX maps with high spatial resolution. Smaller nanoparticles were directly affected by the electron beam, while large particles seemingly stayed unaffected, but the alumina support was damaged, which could change their position during

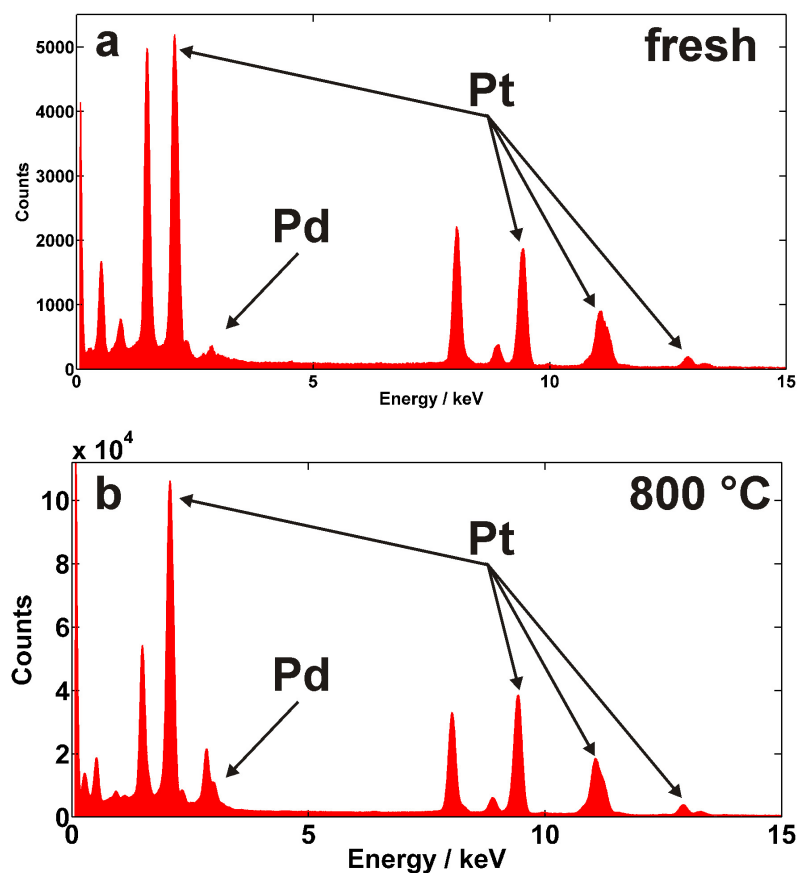


**Figure 5.9:** EDX spectra from large Pt-Pd nanoparticles in the fresh and 800 °C aged samples. The Pt peaks have a similar height, while the Pd-L peak (around 2.8 keV) has a higher intensity in case of the aged specimen.

EDX mapping. Figure 5.10 shows STEM images of a region before and after EDX mapping where strong damage to the alumina support can be seen. The Pt-Pd nanoparticle itself seems mainly unchanged and in this case also stayed in position, but in many cases it would fall off or change its position, rendering the map useless.

The main findings of the last sections are summarised in Table 5.1 to provide an overview. For details, the full texts in the respective sections should be considered. The spatial distribution of the small, medium and large nanoparticles, as well as the chemical composition of the large nanoparticles are shown for each sample.

Particle size	Fresh sample
Small	Dispersed all over the alumina particles
Medium	Concentrated in a layer at the outer edge of the alumina particles
Large	Concentrated in a layer at the outer edge of the alumina particles
Composition	Large NPs are rich in Pt, Pd concentration around 5-10 wt.-%
	<b>Aged at 500 °C</b>
Small	Dispersed all over the alumina particles
Medium	Concentrated in a layer at the outer edge of the alumina particles
Large	Concentrated in a layer at the outer edge of the alumina particles
Composition	Not investigated, likely similar to fresh and 600 °C
	<b>Aged at 600 °C</b>
Small	Dispersed all over the alumina particles
Medium	Mostly disappeared due to sintering
Large	Concentrated in a layer at the outer edge of the alumina particles
Composition	Large NPs are rich in Pt, Pd concentration around 5-10 wt.-%
	<b>Aged at 700 °C</b>
Small	Density strongly reduced due to sintering
Medium	Mostly disappeared due to sintering
Large	Appearing all over the alumina particles
Composition	Large NPs obtain Pd concentrations of 18-30 wt.-%
	<b>Aged at 800 °C</b>
Small	Mostly disappeared due to sintering
Medium	Mostly disappeared due to sintering
Large	Appearing with higher density all over the alumina particles
Composition	NPs from 10-70 nm obtain Pd concentrations of 15-20 wt.-%, a few anomalously NPs (>100 nm) are rich in Pt

**Table 5.1:** Summary of the microstructural changes of the catalyst sample due to ageing. For each ageing temperature, the spatial distribution of the small ( $d < 1.5$  nm), medium-sized ( $1.5 \text{ nm} < d < 10$  nm) and large ( $d > 10$  nm) nanoparticles is described, as well as the chemical composition of the large nanoparticles.

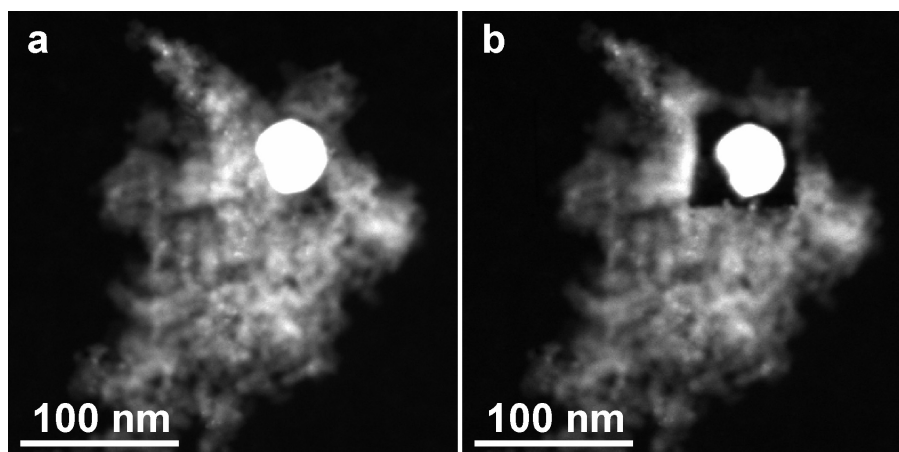


**Figure 5.10:** HAADF-STEM images showing beam damage in a sample region after EDX mapping of a large Pt-Pd nanoparticle. a) Shows the region before, b) after EDX mapping. A rectangular hole in the alumina was created around the nanoparticle.

## 5.6 Surface area measurement (BET method)

The results of the total surface area measurements by the BET method (see Section 3.3) are shown in Table 5.2. The internal surface area of the catalyst was reduced as expected by the ageing. Considerable changes were seen for ageing at 700 °C and 800 °C. These changes are attributed to sintering of the alumina support material.

Sample ageing	BET surface area / (m <sup>2</sup> /g)
Fresh	175
500 °C	162
600 °C	168
700 °C	138
800 °C	122

**Table 5.2:** Results of the BET surface area measurements of the fresh and aged samples. The total internal surface area of the catalyst was reduced during the ageing procedure.

## 5.7 Activity evaluation by CO oxidation

To evaluate the impact of the ageing procedure on the catalytic activity, CO oxidation experiments were performed using the protocol described in Section 3.4. The resulting temperatures versus CO conversion curves for the fresh and aged samples are shown in Figure 5.11. Data are shown from the measurements during one cooling and consecutive heating ramp. The plot for the fresh sample (Figure 5.11a) reveals a two-phase process as the temperature increases. At around 100-110 °C the slope of the curve decreases and increases again around 160 °C, creating almost a saddle point in the plot. Even though the slope of the curve remains positive, this feature will be called a 'dip' in the conversion curve in the following.

A hysteresis can be seen, where the conversion is higher during the cooling ramp at low temperatures, probably caused by CO poisoning of the nanoparticles when starting the ramp at low temperature. Above 125 °C however, the conversion during the heating ramp is slightly higher. The curve approaches full conversion around 280 °C.

The sample aged at 500 °C shows a similar general behaviour, while the conversion is slightly decreased below 100 °C and increased above that temperature compared to the fresh sample. The slope around 100 °C and above is steeper and the dip in the conversion less pronounced. Full conversion is reached at about 230 °C during the heating ramp.

Ageing at 600 °C further increases the slope of the curve between 100 °C and 150 °C, at the same time the hysteresis in that range is increased, while it almost disappears at higher temperatures. The dip in the conversion is further decreased. Full conversion is obtained at 190 °C.

The sample aged at 700 °C exhibits almost no dip in the conversion, has a pronounced hysteresis between 100 °C and 150 °C and reaches almost full conversion already around 175 °C. The low temperature conversion (below 125 °C) though is strongly reduced compared to the previous samples.

Finally, the sample aged at 800 °C deviates from the trend of ageing at lower temperatures. While the low temperature conversion decreases even a bit further, a clear dip in the conversion reappears between 140 °C and 230 °C, after which it reaches 100 %.

One interesting aspect is the strong decrease in the low temperature activity (below 125 °C) after ageing at 700 °C and 800 °C. This was correlated to the onset of severe sintering of the small nanoparticles and clusters after ageing at 700 °C as revealed by the STEM analysis. The low temperature activity is therefore most likely associated with the presence of small nanoparticles and clusters.

The observed two-phase process in the CO oxidation experiments is probably caused by changes in the surface composition of the nanoparticles during the experiments. Possible surface constituents are Pt, Pd and PdO. These can have different

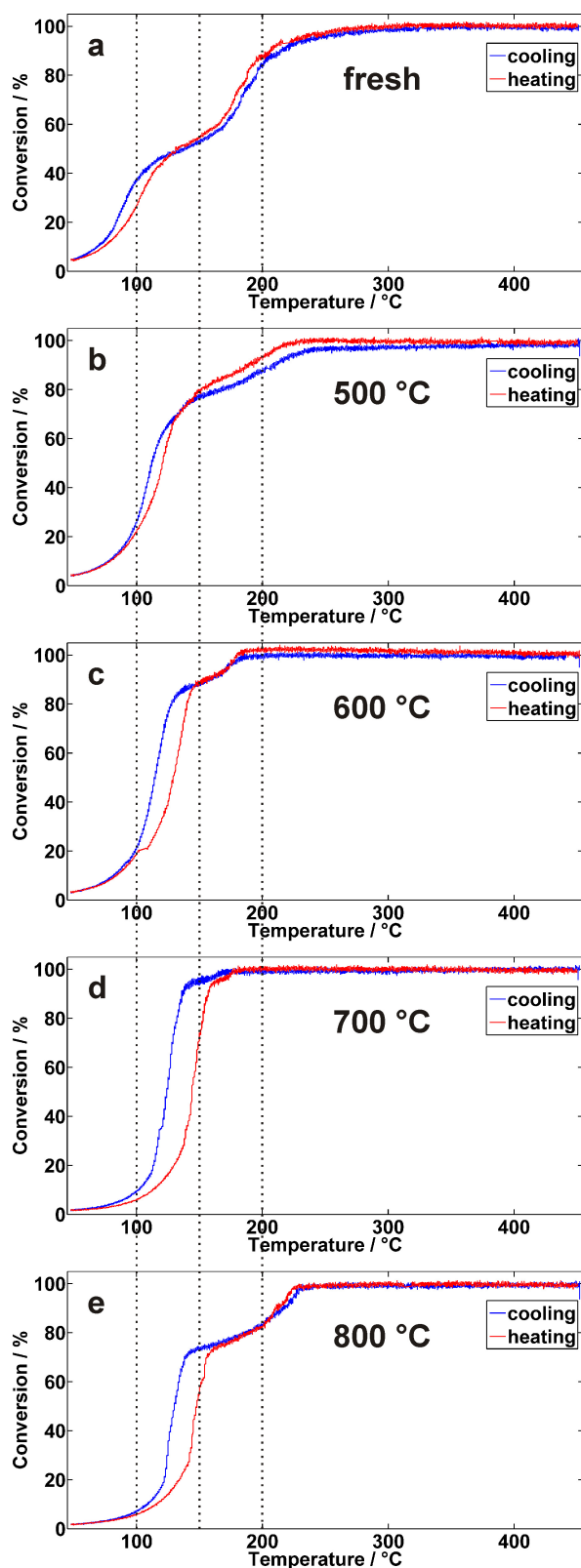


**Figure 5.11:** CO oxidation versus temperature curves for the fresh and aged catalyst samples. The conversion below 100 °C decreases with ageing, while the dip that can be seen for the fresh sample decreases during ageing up to 700 °C. The specimen aged at 800 °C exhibits again a strong dip in the conversion between 140 °C to 230 °C.



CO oxidation activity, where for example PdO appears to have a lower CO oxidation activity compared to Pt [64]. The preferred surface configuration of a Pt-Pd nanoparticle likely depends on the temperature and surrounding gas environment, as well as the nanoparticle size and composition.

More work is needed to further understand this process and the changes in the CO conversion curves induced by ageing. One approach could be a more thorough chemical analysis of the small nanoparticles and dispersed phase, which might reveal more information about the alloying on the nanoscale.

Also, CO oxidation experiments analogue to the ones performed in this work are ongoing using catalysts containing exclusively Pt or Pd (in the same molar concentrations as the bimetallic catalyst). The outcome of these experiments might help to assign certain features observed in the conversion curves to one of the elements and simplify the interpretation.



## 6 Conclusions and outlook

In this thesis, high resolution electron microscopy and spectroscopy were used together with CO oxidation experiments to investigate a bimetallic Pt-Pd/Al<sub>2</sub>O<sub>3</sub> automotive emission catalyst and follow changes induced by high-temperature ageing. A new TEM specimen preparation method was developed that allows the extraction of more representative and quantitative information about particle size distributions compared to traditional methods, and additionally enables the observation of the locations of the nanoparticles in the support structure. While an automotive emission control catalyst is used in this work, the presented method is applicable to many supported nanoparticle catalysts.

Applying this new method, STEM investigations were performed on fresh and aged catalyst samples, complemented by SEM and FIB/SEM experiments. It was found that the fresh specimens contained very small (<1.5 nm) nanoparticles all over the alumina support, while medium-sized (<10 nm) and large nanoparticles (up to 40 nm) were found in an outer layer near the edge of the alumina particles. This observation was backed up by a three-dimensional FIB/SEM slice & view measurement. Upon ageing it was observed that the medium-sized nanoparticles sintered at a temperature around 600 °C, while the small particles remained stable. Ageing at 700 °C induced sintering of the small nanoparticles, while ageing at 800 °C increased the effect of sintering and the number of large nanoparticles above 40 nm.

Chemical characterisation by EDX revealed a change in composition, from Pt rich large nanoparticles and a Pd rich dispersed phase in the fresh specimen to more evenly alloyed nanoparticles after ageing at 700 °C and 800 °C. The microstructural investigations were complemented with catalytic activity tests by means of CO oxidation experiments. The CO conversion versus temperature curves exhibited a two-phase process that is likely due to changes in the surface composition of the bimetallic nanoparticles. After ageing up to 700 °C the CO conversion activity at low temperature (below 125 °C) was reduced, probably caused by sintering of the small nanoparticles, while the activity at temperatures above 125 °C was improved.

Based on the work presented in this thesis, different approaches could be explored to further improve the understanding of the consequences of ageing on the microstructure and activity of supported nanoparticle catalysts. Regarding the samples used for this work, it would be important to obtain a better understanding of the outcome of the CO oxidation experiments and link the observed changes to the microstructure. Reliable EDX spectroscopy data from small nanoparticles or from the finely dispersed phase would help in the understanding. In order to obtain

this data, specialised instrumentation with a higher X-ray detection efficiency needs to be used.

CO oxidation experiments using catalysts containing only Pt or Pd (but otherwise analogue characteristics) are ongoing and might help to identify the role of Pt, Pd and PdO in the observed conversion curves. Once features in these curves can be linked to a certain element, the connection with the microstructure will be further understood.

Besides gaining a better understanding of the investigations performed so far, several new aspects might be explored as well, for example identifying the predominant particle sintering mechanism. Instead of using environmental TEM, which incorporates the risk of beam damage during the experiment and unrealistic ageing conditions (low pressure), TEM specimen grids that allow locating certain specimen regions could be used to image a region of the specimen, remove it from the instrument, perform an ageing treatment, and then image the same region again. The changes observed in this region could allow conclusions about the mechanism of particle sintering.

One further aspect of interest is the character of the nanoparticle-support interaction (e.g. contact angle), including changes due to ageing treatments or differences between different support structures. Since the support material stabilises the nanoparticles and should influence their sintering behaviour, the interaction properties are of fundamental interest. For investigations of fundamental properties of individual nanoparticles, the use of support structures with a less complex geometry would be beneficial and simplify the experimental work. So instead of using a porous  $\gamma$ -Al<sub>2</sub>O<sub>3</sub> support, a model system could be used. Possible candidates are small, platelet-shaped  $\gamma$ -Al<sub>2</sub>O<sub>3</sub> nanoparticles or needle-shaped alumina structures which would allow imaging of the contact region between the alumina and the supported nanoparticles.

# Acknowledgments

The research presented in this thesis was carried out in the Division of Microscopy & Microanalysis and in the Eva Olsson Group in the Department of Applied Physics, as well as in the Competence Centre for Catalysis (KCK), Chalmers University of Technology, Gothenburg, Sweden, during the period of September 2011 to January 2015. The work was performed under the supervision of Prof. Eva Olsson and co-supervisors Prof. Magnus Skoglundh and Prof. Henrik Grönbeck.

The Competence Centre for Catalysis is hosted by Chalmers University of Technology and financially supported by the Swedish Energy Agency and the member companies AB Volvo, ECAPS AB, Haldor Topsøe A/S, Scania CV AB, Volvo Car Corporation AB and Wärtsilä Finland Oy.

Funding for the electron microscopes by the Knut and Alice Wallenberg Foundation and Vetenskapsrådet is gratefully acknowledged.

Additionally I would like to express my gratitude to:

My main supervisor Prof. Eva Olsson for all your help, guidance and outstanding support throughout my project, both in practical issues like introduction to techniques and writing, as well as finding new ways and ideas.

My co-supervisors Prof. Magnus Skoglundh and Prof. Henrik Grönbeck for many fruitful discussion, new ideas and support.

All members of the Eva Olsson Group, the Division of Materials Microstructure, the Chalmers Materials Analysis Laboratory and the former Division of Microscopy and Microanalysis for a great work (and fika) climate, a lot of support and nice activities outside of work. Special thanks go to Anna Jansson, my great office mate, for a lot of help and especially nice conversations and cheering-up on early mornings (haha) and late evenings, Olof Bäcké for his friendship, nice game sessions and permanent support, 'the honeys' Samira Nik and Nikolina Tuzla for always being in a good mood and providing entertainment during the coffee breaks, Amine Yousfi, my personal gym motivator, Lunjie Zeng, Stefan Gustafsson and Charlotte Hamngren Blomqvist for many nice conversations and company, Ola Löfgren for all the technical support and Anders Kvist for the help with countless small and large problems.

All members of KCK for giving me an insight into different aspects of catalysis and nice company during conferences and summer schools. Special thanks go to Pooya Tabib Zadeh Adibi for friendship, guitar sessions and nice dinners, and Sheedeh Fouladvand for our collaborations and her support.

Carl Wadell for his friendship, our collaboration and the fun activities outside of work.

Last but not least, a big thanks to my family and my girlfriend Hanna for all their love and great support.

# Bibliography

- [1] R. M. Heck, R. J. Farrauto, and S. T. Gulati. *Catalytic Air Pollution Control*. Wiley, 2009.
- [2] A. Chaloulakou, I. Mavroidis, and I. Gavriil. Compliance with the annual NO<sub>2</sub> air quality standard in athens. required NO<sub>x</sub> levels and expected health implications. *Atmospheric Environment*, 42(3), 454–465, 2008.
- [3] D. L. Mauzerall, B. Sultan, N. Kim, and D. F. Bradford. NO<sub>x</sub> emissions from large point sources: variability in ozone production, resulting health damages and economic costs. *Atmospheric Environment*, 39(16), 2851–2866, 2005.
- [4] Euro 5 / Euro 6 emission regulations. <http://eur-lex.europa.eu/legal-content/EN/ALL/?uri=CELEX:32007R0715>. Accessed: 2014-11-30.
- [5] C. D. Falk and J. J. Mooney. Three-way conversion catalysts: Effect of closed-loop feed-back control and other parameters on catalyst efficiency, 1980. SAE International.
- [6] G. Liu and P.-X. Gao. A review of NO<sub>x</sub> storage/reduction catalysts: mechanism, materials and degradation studies. *Catalysis Science & Technology*, 1(4), 552, 2011.
- [7] S. Roy and A. Baiker. NO<sub>x</sub> storage-reduction catalysis: from mechanism and materials properties to storage-reduction performance. *Chemical Reviews*, 109(9), 4054–91, 2009. Roy, Sounak Baiker, Alfons Chem Rev. 2009 Sep;109(9):4054-91. read.
- [8] C. H. Bartholomew. Mechanisms of catalyst deactivation. *Applied Catalysis A: General*, 212(1-2), 17–60, 2001.
- [9] P. Forzatti and L. Lietti. Catalyst deactivation. *Catalysis Today*, 52(2–3), 165–181, 1999.
- [10] F. Eigenmann, M. Maciejewski, and A. Baiker. Gas adsorption studied by pulse thermal analysis. *Thermochimica Acta*, 359(2), 131–141, 2000.
- [11] T. Lear, N. G. Hamilton, and D. Lennon. The application of temperature-programmed desorption, adsorption isotherms and temperature-programmed

- oxidation to investigate the interaction of CO with alumina-supported palladium catalysts. *Catalysis Today*, 126(1–2), 219–227, 2007.
- [12] J. Dawody, L. Eurenus, H. Abdulhamid, M. Skoglundh, E. Olsson, and E. Fridell. Platinum dispersion measurements for Pt/BaO/Al<sub>2</sub>O<sub>3</sub> NO<sub>x</sub> storage catalysts. *Applied Catalysis A: General*, 296(2), 157–168, 2005.
- [13] C. Karakaya and O. Deutschmann. A simple method for CO chemisorption studies under continuous flow: Adsorption and desorption behavior of Pt/Al<sub>2</sub>O<sub>3</sub> catalysts. *Applied Catalysis A: General*, 445–446(0), 221–230, 2012.
- [14] H. Dropsch and M. Baerns. CO adsorption on supported Pd catalysts studied by adsorption microcalorimetry and temperature programmed desorption. *Applied Catalysis A: General*, 158(1–2), 163–183, 1997.
- [15] M.-K. Min, J. Cho, K. Cho, and H. Kim. Particle size and alloying effects of Pt-based alloy catalysts for fuel cell applications. *Electrochimica Acta*, 45(25–26), 4211–4217, 2000.
- [16] R. M. Rioux, H. Song, J. D. Hoefelmeyer, P. Yang, and G. A. Somorjai. High-surface-area catalyst design: synthesis, characterization, and reaction studies of platinum nanoparticles in mesoporous SBA-15 silica. *The Journal of Physical Chemistry B*, 109(6), 2192–2202, 2004.
- [17] S. Damyanova and J. M. C. Bueno. Effect of CeO<sub>2</sub> loading on the surface and catalytic behaviors of CeO<sub>2</sub>-Al<sub>2</sub>O<sub>3</sub>-supported Pt catalysts. *Applied Catalysis A: General*, 253(1), 135–150, 2003.
- [18] R. Srinivasan and B. H. Davis. X-ray diffraction and electron microscopy studies of platinum-tin-silica catalysts. *Applied Catalysis A: General*, 87(1), 45–67, 1992.
- [19] I. Chorkendorff and J. W. Niemantsverdriet. *Concepts of Modern Catalysis and Kinetics*. Wiley, 2007.
- [20] 50by50 global fuel economy initiative. [http://www.globalfueleconomy.org/Documents/Publications/50BY50\\_report.pdf](http://www.globalfueleconomy.org/Documents/Publications/50BY50_report.pdf). Accessed: 2015-01-12.
- [21] European vehicle market statistics. [http://www.theicct.org/sites/default/files/publications/EU\\_vehiclemarket\\_pocketbook\\_2013\\_Web.pdf](http://www.theicct.org/sites/default/files/publications/EU_vehiclemarket_pocketbook_2013_Web.pdf). Accessed: 2015-01-12.
- [22] Nacs news. <http://www.nacsonline.com/news/daily/pages/nd0714143.aspx>. Accessed: 2015-01-12.



- 
- [23] Euro 1 emission regulation. <http://eur-lex.europa.eu/legal-content/EN/ALL/?uri=CELEX:31991L0441>. Accessed: 2014-11-30.
- [24] Euro 2 emission regulation. <http://eur-lex.europa.eu/legal-content/EN/ALL/?uri=CELEX:32002L0051>. Accessed: 2014-11-30.
- [25] Euro 3 / Euro 4 emission regulations. <http://eur-lex.europa.eu/legal-content/EN/ALL/?uri=CELEX:31998L0069>. Accessed: 2014-11-30.
- [26] S. J. Tauster, S. C. Fung, R. T. K. Baker, and J. A. Horsley. Strong interactions in supported-metal catalysts. *Science*, 211, 1121, 1981.
- [27] P. Loof, B. Stenbom, H. Norden, and B. Kasemo. Rapid sintering in NO of nanometer-sized Pt particles on gamma-Al<sub>2</sub>O<sub>3</sub> observed by CO temperature-programmed desorption and transmission electron microscopy. *Journal of Catalysis*, 144(1), 60–76, 1993.
- [28] D. J. Smith, D. White, T. Baird, and J. R. Fryer. The characterisation of a model platinum/alumina catalyst by high-resolution electron microscopy. *Journal of Catalysis*, 81(1), 107–118, 1983.
- [29] X. Chen, Y. Cheng, C. Y. Seo, J. W. Schwank, and R. W. McCabe. Aging, re-dispersion, and catalytic oxidation characteristics of model Pd/Al<sub>2</sub>O<sub>3</sub> automotive three-way catalysts. *Applied Catalysis B: Environmental*, 163, 499–509, 2015.
- [30] J. Barbier Jr and D. Duprez. Steam effects in three-way catalysis. *Applied Catalysis B: Environmental*, 4(2–3), 105–140, 1994.
- [31] S. B. Simonsen, I. Chorkendorff, S. Dahl, M. Skoglundh, J. Sehested, and S. Helveg. Direct observations of oxygen-induced platinum nanoparticle ripening studied by In Situ TEM. *Journal of the American Chemical Society*, 132(23), 7968–7975, 2010.
- [32] A. T. DeLaRiva, T. W. Hansen, Sivakumar R. Challa, and A. K. Datye. In situ transmission electron microscopy of catalyst sintering. *Journal of Catalysis*, 308(0), 291–305, 2013.
- [33] A. Bellare, D. B. Dadyburjor, and M. J. Kelley. Evolution of bimodal distributions in the sintering of model supported metal catalysts. *Journal of Catalysis*, 117(1), 78–90, 1989.
- [34] R. J. Liu, P. A. Crozier, C. M. Smith, D. A. Hucul, J. Blackson, and G. Salaita. In situ electron microscopy studies of the sintering of palladium nanoparticles on alumina during catalyst regeneration processes. *Microsc Microanal*, 10(1), 77–85, 2004.

- [35] A. K. Datye, Q. Xu, K. C. Kharas, and J. M. McCarty. Particle size distributions in heterogeneous catalysts: What do they tell us about the sintering mechanism? *Catalysis Today*, 111(1-2), 59–67, 2006.
- [36] S. E. Wanke and P. C. Flynn. The sintering of supported metal catalysts. *Catalysis Reviews*, 12(1), 93–135, 1975.
- [37] M. Ozawa, T. Okouchi, and M. Haneda. Three way catalytic activity of thermally degenerated Pt/Al<sub>2</sub>O<sub>3</sub> and Pt/CeO<sub>2</sub>-ZrO<sub>2</sub> modified Al<sub>2</sub>O<sub>3</sub> model catalysts. *Catalysis Today*, 242, Part B, 329–337, 2015.
- [38] Y. Ji, V. Easterling, U. Graham, C. Fisk, M. Crocker, and J.-S. Choi. Effect of aging on the NO<sub>x</sub> storage and regeneration characteristics of fully formulated lean NO<sub>x</sub> trap catalysts. *Applied Catalysis B: Environmental*, 103(3-4), 413–427, 2011.
- [39] A. Russell and W. S. Epling. Diesel oxidation catalysts. *Catalysis Reviews*, 53(4), 337–423, 2011.
- [40] N. Takahashi and H. Imagawa. Improvement of catalysts for NO<sub>x</sub> storage and reduction for gasoline-fueled automotive exhaust. *Journal of the Japan Petroleum Institute*, 52(3), 90–101, 2009.
- [41] S. Benramdhane, C.-N. Millet, E. Jeudy, J. Lavy, V. B. Aube, and M. Daturi. Impact of thermal and vehicle aging on the structure and functionalities of a lean NO<sub>x</sub>-trap. *Catalysis Today*, 176(1), 56–62, 2011.
- [42] A. Morlang, U. Neuhausen, K. V. Klementiev, F. W. Schütze, G. Miehe, H. Fuess, and E. S. Lox. Bimetallic Pt/Pd diesel oxidation catalysts: Structural characterisation and catalytic behaviour. *Applied Catalysis B: Environmental*, 60(3-4), 191–199, 2005.
- [43] O. K. Ezekoye, A. R. Drews, H. W. Jen, R. J. Kudla, R. W. McCabe, M. Sharma, J. Y. Howe, L. F. Allard, G. W. Graham, and X. Q. Pan. Characterization of alumina-supported Pt and Pt–Pd NO oxidation catalysts with advanced electron microscopy. *Journal of Catalysis*, 280(1), 125–136, 2011.
- [44] G. W. Graham, H. W. Jen, O. Ezekoye, R. J. Kudla, W. Chun, X. Q. Pan, and R. W. McCabe. Effect of alloy composition on dispersion stability and catalytic activity for NO oxidation over alumina-supported Pt–Pd catalysts. *Catalysis Letters*, 116(1-2), 1–8, 2007.
- [45] K. Kallinen, A. Moreno, A. Savimäki, and T. J. J. Kinnunen. Pt/Pd diesel oxidation catalyst : A study on the properties enhanced by the use of Pd, 2009. SAE Technical Paper 2009-26-0018.

- 
- [46] C. H. Kim, M. Schmid, S. J. Schmieg, J. Tan, and W. Li. The effect of Pt-Pd ratio on oxidation catalysts under simulated diesel exhaust, 2011. SAE Technical Paper 2011-01-1134.
- [47] M. R. Ward, T. Hyde, E. D. Boyes, and P. L. Gai. Nanostructural studies of fresh and road-aged practical Pt/SiO<sub>2</sub> and Pt-Pd/Al<sub>2</sub>O<sub>3</sub> diesel oxidation catalysts by using aberration-corrected (scanning) transmission electron microscopy. *ChemCatChem*, 4(10), 1622–1631, 2012.
- [48] T. R. Johns, J. R. Gaudet, E. J. Peterson, J. T. Miller, E. A. Stach, C. H. Kim, M. P. Balogh, and A. K. Datye. Microstructure of bimetallic Pt-Pd catalysts under oxidizing conditions. *ChemCatChem*, 5(9), 2636–2645, 2013.
- [49] J. Andersson, M. Antonsson, L. Eurenium, E. Olsson, and M. Skoglundh. Deactivation of diesel oxidation catalysts: Vehicle- and synthetic aging correlations. *Applied Catalysis B: Environmental*, 72(1–2), 71–81, 2007.
- [50] J. Goldstein, D. E. Newbury, D. C. Joy, C. E. Lyman, P. Echlin, E. Lifshin, L. Sawyer, and J. R. Michael. *Scanning Electron Microscopy and X-ray Microanalysis*. Springer, 2003.
- [51] David B. Williams and C. Barry Carter. *Transmission Electron Microscopy*. Springer, 2009.
- [52] S. J. Pennycook and P. D. Nellist. *Scanning Transmission Electron Microscopy - Imaging and Analysis*. Springer, 2011.
- [53] P. Hartel, H. Rose, and C. Dinges. Conditions and reasons for incoherent imaging in STEM. *Ultramicroscopy*, 63(2), 93–114, 1996.
- [54] M. Haider, S. Uhlemann, E. Schwan, H. Rose, B. Kabius, and K. Urban. Electron microscopy image enhanced. *Nature*, 392(6678), 768–769, 1998.
- [55] W. S Rasband. Imagej, <http://imagej.nih.gov/ij/>, 1997-2015.
- [56] M. H. F. Overwijk, F. C. van den Heuvel, and C. W. T. Bulle-Lieuwma. Novel scheme for the preparation of transmission electron microscopy specimens with a focused ion beam. *Journal of Vacuum Science & Technology B*, 11(6), 2021–2024, 1993.
- [57] R. M. Langford and C. Clinton. In situ lift-out using a FIB-SEM system. *Micron*, 35(7), 607–611, 2004.
- [58] D. Bounechada, S. Fouladvand, L. Kylhammar, T. Pingel, E. Olsson, M. Skoglundh, J. Gustafson, M. Di Michiel, M. A. Newton, and P.-A. Carlsson. Mechanisms behind sulfur promoted oxidation of methane. *Physical Chemistry Chemical Physics*, 2013.

- [59] T. Lesage, J. Saussey, S. Malo, M. Hervieu, C. Hedouin, G. Blanchard, and M. Daturi. Operando FTIR study of  $\text{NO}_x$  storage over a Pt/K/Mn/ $\text{Al}_2\text{O}_3$ - $\text{CeO}_2$  catalyst. *Applied Catalysis B: Environmental*, 72(1–2), 166–177, 2007.
- [60] H. Kannisto, H. H. Ingelsten, and M. Skoglundh. Ag- $\text{Al}_2\text{O}_3$  catalysts for lean  $\text{NO}_x$  reduction—influence of preparation method and reductant. *Journal of Molecular Catalysis A: Chemical*, 302(1–2), 86–96, 2009.
- [61] Z. Huang, J. R. Fryer, C. Park, D. Stirling, and G. Webb. Transmission electron microscopy and energy dispersive X-ray spectroscopy studies of Pt-Sn/ $\gamma$ - $\text{Al}_2\text{O}_3$  catalysts. *Journal of Catalysis*, 159(2), 340–352, 1996.
- [62] E. D. Boyes, M. R. Ward, L. Lari, and P. L. Gai. ESTEM imaging of single atoms under controlled temperature and gas environment conditions in catalyst reaction studies. *Annalen der Physik*, 525(6), 423–429, 2013.
- [63] P. L. Gai, L. Lari, M. R. Ward, and E. D. Boyes. Visualisation of single atom dynamics and their role in nanocatalysts under controlled reaction environments. *Chemical Physics Letters*, 592(0), 355–359, 2014.
- [64] H. Gabasch, A. Knop-Gericke, R. Schlögl, M. Borasio, C. Weilach, G. Rupprechter, S. Penner, B. Jenewein, K. Hayek, and B. Klotzer. Comparison of the reactivity of different Pd-O species in CO oxidation. *Phys. Chem. Chem. Phys.*, 9, 533–540, 2007.